Observing the Galaxy's massive black hole with gravitational wave bursts

C. P. L. Berry[1]* and J. R. Gair[1]

[1]*Institute of Astronomy, University of Cambridge, Madingley Road, Cambridge, CB3 0HA*

7 August 2012

ABSTRACT

An extreme-mass-ratio burst (EMRB) is a gravitational wave signal emitted when a solar mass compact object on a highly eccentric orbit about a much more massive object, such as a $10^6 M_\odot$ black hole, passes through periapsis. EMRBs are a relatively unexplored means of probing the spacetime of the massive black hole in the Galaxy's core. We conduct a preliminary investigation of the properties of EMRBs and how they could allow us to constrain the massive black hole's parameters, such as its spin. We find that EMRBs should be detectable if their periapse distance is less than $65r_{\rm g}$ for a $\mu = 10 M_\odot$ orbiting object, where $r_{\rm g} = GM_\bullet/c^2$ is the gravitational radius. The signal-to-noise ratio scales approximately as $\log(\rho) \simeq -2.7\log(r_{\rm p}/r_{\rm g}) + \log(\mu/M_\odot) + 4.9$. For periapses smaller than ... EMRBs can informative, and provide constraints on both the massive black hole's mass and spin. Closer orbits provide better constraints, with the best giving accuracies of better than one part in 10^4 for both the mass and spin parameter.

Key words: black hole physics – Galaxy: centre – gravitational waves – methods: data analysis.

1 BACKGROUND AND INTRODUCTION

Many, if not all, galactic nuclei have harboured a massive black hole (MBH) during their evolution (Lynden-Bell & Rees 1971; Sołtan 1982; Rees 1984). Observations have shown there exist well-defined correlations between the MBHs' masses and the properties of their host galaxies, such as bulge luminosity, mass, velocity dispersion and light concentration (Kormendy & Richstone 1995; Magorrian et al. 1998; Ferrarese & Merritt 2000; Gebhardt et al. 2000; Graham et al. 2001; Tremaine et al. 2002; Marconi & Hunt 2003; Häring & Rix 2004; Graham 2007; Graham et al. 2011). These suggest coeval evolution of the MBH and galaxy (Peng 2007; Jahnke & Macciò 2011), possibly with feedback mechanisms coupling the two (Haiman & Quataert 2004; Volonteri & Natarajan 2009). The MBH and the surrounding spheroidal galaxy share a common history, such that the growth of one can inform us about the growth of the other.

The best opportunity to study MBHs comes from the compact object in our own galactic centre (GC), which is coincident with Sagittarius A* (Sgr A*). This is identified as an MBH of mass $M_\bullet = 4.31 \times 10^6 M_\odot$ at a distance of only $R_0 = 8.33$ kpc (Gillessen et al. 2009).

According to the no-hair theorem, the MBH should be described completely by just its mass $M_\bullet$ and spin a, since we expect the charge of an astrophysical black hole to be negligible (Israel 1967, 1968; Carter 1971; Hawking 1972; Robinson 1975; Chandrasekhar 1998). The spin parameter a is related to the BH's angular momentum J by

$$J = M_\bullet a c; \tag{1}$$

it is often convenient to use the dimensionless spin

$$a_* = \frac{cJ}{GM_\bullet^2}. \tag{2}$$

As we have a good estimate of the mass, to gain a complete description of the MBH we have only to measure its spin; this shall give us insight into its history and role in the evolution of the Galaxy.

The spin of an MBH is determined by several competing processes. An MBH accumulates mass and angular momentum through accretion (Volonteri 2010). Accretion from a gaseous disc shall spin up the MBH, potentially leading to high spin values (Volonteri et al. 2005), while a series of randomly oriented accretion events shall lead to a low spin value: we expect an average value $|a_*| \sim 0.1$–0.3 (King & Pringle 2006; King, Pringle & Hofmann 2008). The MBH shall also grow through mergers (Yu & Tremaine 2002; Malbon et al. 2007). Minor mergers with smaller black holes (BHs) can decrease the spin (Hughes & Blandford 2003; Gammie, Shapiro & McKinney 2004), while a series

* E-mail: cplb2@cam.ac.uk

of major mergers, between similar mass MBHs, would lead to a likely spin of $|a_*| \sim 0.69$ (Berti & Volonteri 2008; Berti et al. 2007; González et al. 2007). Measuring the spin of MBHs shall help us understand the relative importance of these processes, and perhaps gain a glimpse into their host galaxies' pasts.

Elliptical and spiral galaxies are believed to host MBHs of differing spins because of their different evolutions: we expect MBHs in elliptical galaxies to have on average higher spins than black holes in spiral galaxies, where random, small accretion episodes have played a more important role (Volonteri, Sikora & Lasota 2007; Sikora, Stawarz & Lasota 2007).

It has been suggested that the spin of the Galaxy's MBH could be inferred from careful observation of the orbits of stars within a few milliparsecs of the GC (Merritt et al. 2010), although this is complicated because of perturbations due to other stars, or from observations of quasi-periodic oscillations (QPOs) in the luminosity of flares believed to originate from material orbiting close to the innermost stable orbits (Genzel et al. 2003; Bélanger et al. 2006; Trippe et al. 2007; Hamaus et al. 2009; Kato et al. 2010), though there are difficulties in interpreting these results (Psaltis 2008).

This latter method, combined with a disc-seismology model, has produced a value of the dimensionless spin of $a_* = 0.44 \pm 0.08$. To obtain this result Kato et al. (2010) have combined their observations of Sgr A* with observations of galactic X-ray sources containing solar mass BHs, to find a best-fit unique spin parameter for all BHs. However, it is not clear that all BHs should share the same value of the spin parameter; especially considering that the BHs considered here differ in mass by six orders of magnitude, with none in the intermediate range. Even if BH spin is determined by a universal process, we still expect some distribution of spin parameters (King et al. 2008; Berti & Volonteri 2008). Thus we cannot precisely determine the spin of the galactic centre's MBH from an average including other BHs.

The spins of MBHs in active galactic nuclei have been inferred using X-ray observations of Fe K emission lines (Miller 2007; McClintock et al. 2011). So far this has been done for a handful of other galaxies' central MBHs (Brenneman & Reynolds 2006; Miniutti et al. 2009; Schmoll et al. 2009; de la Calle Pérez et al. 2010; Zoghbi et al. 2010; Nardini et al. 2011; Patrick et al. 2011). Estimates for the spin cover a range of values up to the maximal value for an extremal Kerr black hole. Typical values are in the intermediate range of $a_* \sim 0.7$ with an uncertainty of about 10% on each measurement.

While we can use the spin of other BHs as a prior, to inform us of what we should expect to measure for the spin of the Galaxy's MBH, it is desirable to have an independent observation, a direct measurement.

An exciting means of inferring information about the MBH is through gravitational waves (GWs) emitted when compact objects (COs), such as stellar mass BHs, neutron stars (NSs), white dwarfs (WDs) or low mass main sequence (MS) stars, pass close by (Sathyaprakash & Schutz 2009). A space-borne detector, such as the *L*aser Interferometer Space Antenna (LISA) or the *e*volved Laser Interferometer Space Antenna (eLISA), is designed to be able to detect GWs in the frequency range of interest for these encounters (Bender et al. 1998; Danzmann & Rüdiger 2003;

Jennrich et al. 2011; Amaro-Seoane et al. 2012).[1] The identification of waves requires a set of accurate waveform templates covering parameter space. Much work has already been done on the waveforms generated when companion objects inspiral towards an MBH (Glampedakis 2005); as they orbit, the GWs carry away energy and angular momentum, causing the orbit to shrink until eventually the object plunges into the MBH. The initial orbits may be highly elliptical and a burst of radiation is emitted during each close encounter. These are known as extreme mass-ratio bursts (EMRBs; Rubbo et al. 2006). Assuming that the companion is not scattered from its orbit, and does not plunge straight into the MBH, its orbit shall evolve, becoming more circular, and it shall begin to continuously emit significant gravitational radiation in the LISA/eLISA frequency range. The resulting signals are known as extreme mass-ratio inspirals (EMRIs; Amaro-Seoane et al. 2007).

Studies of these systems have usually focused upon when the orbit completes multiple cycles, allowing a high signal-to-noise ratio (SNR) to be accumulated. Here, we investigate high eccentricity orbits. These are the initial bursting orbits from which an EMRI may evolve. The event rate for the detection of such EMRBs with LISA has been estimated to be as high as 15 yr^{-1} (Rubbo, Holley-Bockelmann & Finn 2006), although this has been subsequently revised downwards to the order of 1 yr^{-1} (Hopman, Freitag & Larson 2007). Even if only a single burst is detected during a mission, this is still an exciting possibility since the information carried by the GW should give an unparalleled probe of the structure of spacetime of the GC. Exactly what can be inferred depends upon the orbit.

We make the simplifying assumption that all these orbits are marginally bound, or parabolic, since highly eccentric orbits appear almost indistinguishable from an appropriate parabolic orbit. Here "parabolic" and "eccentricity" refer to the energy of the geodesic and not to the geometric shape of the orbit.[2] Following such a trajectory an object may make just one pass of the MBH or, if the periapsis distance is small enough, it may complete a number of rotations. Such an orbit is referred to as zoom-whirl (Glampedakis & Kennefick 2002).

In order to compute the gravitational waveform produced in such a case, we integrate the geodesic equations for a parabolic orbit in Kerr spacetime. We assume that the orbiting body is a test particle, such that it does not influence the underlying spacetime, and that the orbital parameters evolve negligibly during the orbit such that they may be held constant. We use this to construct an approximate numerical kludge waveform (Babak et al. 2007).

This paper is organised as follows. We being in Sec. 2 with the construction of the geodesic orbits, these trajectories are used in the construction of NK waveforms as explained in Sec. 3. In Sec. 4 we establish what the LISA detectors would measure, and in Sec. 5 how the signal would be

---

[1] The revised eLISA concept shares the same descoped design as the *N*ew Gravitational-wave Observatory (NGO) submitted to the European Space Agency for their L1 mission selection.
[2] Marginally bound Keplerian orbits in flat spacetime are parabolic in both senses.

analysed. This includes a brief mention of window functions, which is expanded in Appendix A, where we also present a novel window function, the Planck-Bessel window, which may be of use for signals with a large dynamic range. In Sec. 6 we look at the our NK waveforms. We give fiducial power-law fits for SNR as a function of periapse radius, which may be of use for back-of-the-envelope estimates. We confirm the accuracy of the kludge waveforms in Sec. 7 by comparing the energy flux to fluxes calculated using other approaches. The typical error introduced by the NK approximation may be a few percent, but this worsens when the periapses approaches the last non-plunging orbit. We explain how to extract the information from the bursts in Sec. 8. Results estimating the accuracy to which parameters could be measured are presented in Sec. 9. We briefly mention the possibility of detecting bursts from extra-galactic sources in Sec. 10, before concluding in Sec. 11 with a summary of our results. EMRBs may be informative if the event rate is high enough for them to be a viable source.

There are currently no confirmed space-borne detector missions. We shall use the classic LISA design for this study. This is done from historical affection in lieu of a definite alternative. Should funding for a space-borne detector be secured in the future it is hoped that it shall have comparable sensitivity to LISA, and that studies using the LISA design shall be a sensible benchmark for comparison.

Throughout this work we adopt a metric with signature $(+, -, -, -)$. Greek indices are used to represent spacetime indices $\mu = \{0, 1, 2, 3\}$ and lowercase Latin indices from the middle of the alphabet are used for spatial indices $i = \{1, 2, 3\}$. Uppercase Latin indices from the beginning of the alphabet are used for the output of the two LISA detector-arms $A = \{\mathrm{I}, \mathrm{II}\}$, and lowercase Latin indices from the beginning of the alphabet are used for parameter space. Summation over repeated indices is assumed unless explicitly noted otherwise. Geometric units with $G = c = 1$ are where noted, but in general factors of G and c are retained.

2   PARABOLIC ORBITS IN KERR SPACETIME

2.1   The metric and geodesic equations

Astrophysical BHs are described by the Kerr metric (Kerr 1963). In standard Boyer-Lindquist coordinates the line element is (Boyer & Lindquist 1967; Hobson, Efstathiou & Lasenby 2006, section 13.7)

$$ds^2 = \frac{\rho^2 \Delta}{\Sigma^2} c^2 dt^2 - \frac{\Sigma \sin^2 \theta}{\rho^2} (d\phi - \omega dt)^2 - \frac{\rho^2}{\Delta} dr^2 - \rho^2 d\theta^2, \quad (3)$$

where we have introduced functions

$$\rho^2 = r^2 + a^2 \cos^2 \theta, \quad (4)$$

$$\Delta = r^2 - \frac{2GM_\bullet r}{c^2} + a^2, \quad (5)$$

$$\Sigma = (r^2 + a^2)^2 - a^2 \Delta \sin^2 \theta, \quad (6)$$

$$\omega = \frac{2GM_\bullet ar}{c\Sigma}. \quad (7)$$

For the remainder of this section we shall work in natural units with $G = c = 1$.

Geodesics are parametrized by three conserved quantities (aside from the particle's mass μ): energy (per unit mass) E, specific angular momentum about the symmetry axis (the z-axis) L_z, and Carter constant Q (Carter 1968; Chandrasekhar 1998, section 62). The geodesic equations are

$$\rho^2 \frac{dt}{d\tau} = a \left(L_z - aE \sin^2 \theta \right) + \frac{r^2 + a^2}{\Delta} T, \quad (8)$$

$$\rho^2 \frac{dr}{d\tau} = \pm \sqrt{V_r}, \quad (9)$$

$$\rho^2 \frac{d\theta}{d\tau} = \pm \sqrt{V_\theta}, \quad (10)$$

$$\rho^2 \frac{d\phi}{d\tau} = \frac{L_z}{\sin^2 \theta} - aE + \frac{a}{\Delta} T, \quad (11)$$

where we have introduced potentials

$$T = E \left(r^2 + a^2 \right) - aL_z, \quad (12)$$

$$V_r = T^2 - \Delta \left[r^2 + (L_z - aE)^2 + Q \right], \quad (13)$$

$$V_\theta = Q - \cos^2 \theta \left[a^2 \left(1 - E^2 \right) + \frac{L_z^2}{\sin^2 \theta} \right], \quad (14)$$

and τ is proper time. The signs of the r and θ equations may be chosen independently.

For a parabolic orbit $E = 1$; the particle is at rest at infinity. This simplifies the geodesic equations. It also allows us to give a simple interpretation for the Carter constant: this is defined as

$$Q = L_\theta^2 + \cos^2 \theta \left[a^2 \left(1 - E^2 \right) + \frac{L_z^2}{\sin^2 \theta} \right], \quad (15)$$

where L_θ is the (non-conserved) specific angular momentum in the θ-direction ($V_\theta = L_\theta^2$). For $E = 1$ we have

$$Q = L_\theta^2 + \cot^2 \theta \, L_z^2 = L_\infty^2 - L_z^2; \quad (16)$$

here L_∞ is the total specific angular momentum at infinity, where the metric is asymptotically flat (de Felice 1980).[3] This is as in Schwarzschild spacetime.

2.2   Integration variables and turning points

In integrating the geodesic equations, difficulties can arise because of the presence of turning points in the motion, when the sign of the r or θ geodesic equation shall change. The radial turning points are at the periapsis r_p and at infinity. We may locate the periapsis by finding the roots of

$$V_r = 2M_\bullet r^3 - \left(L_z^2 + Q \right) r^2 + 2M_\bullet \left[(L_z - a)^2 + Q \right] r - a^2 Q$$
$$= 0. \quad (17)$$

This has three roots, which we shall denote $\{r_1, r_2, r_\mathrm{p}\}$; the periapsis r_p is the largest real root. We do not find the apoapsis as a (fourth) root to this equation as we have removed it by taking $E = 1$ before solving. This turning point can be found by setting the unconstrained expression for V_r equal to zero, and then solving for $E(r)$; taking the limit $r \to \infty$ gives $E \to 1$ (Wilkins 1972).

---

[3] See Rosquist, Bylund & Samuelsson (2009) for a discussion of the interpretation of Q in the limit $G \to 0$, corresponding to a flat spacetime.
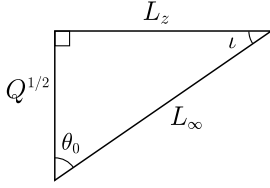
Figure 1. The angular momenta L_∞, L_z and $\sqrt{Q}$ define a right-angled triangle. The acute angles are θ_0, the extremal value of the polar angle, and ι, the orbital inclination (Glampedakis, Hughes & Kennefick 2002).

We may avoid the difficulties associated with the turning point by introducing an angular variable that always increases with proper time (Drasco & Hughes 2004): inspired by Keplerian orbits, we parametrize our trajectory by

$$r = \frac{p}{1 + e\cos\psi}, \tag{18}$$

where $e = 1$ is the eccentricity and $p = 2r_{\rm p}$ is the semilatus rectum. As ψ covers its full range from $-\pi$ to π, r traces out one complete orbit from infinity through the periapsis at $\psi = 0$ back to infinity. The geodesic equation for ψ is

$$\rho^2 \frac{d\psi}{d\tau} = \left\{ M_\bullet \left[2r_{\rm p} - (r_1 + r_2)(1 + \cos\psi) \right. \right.$$
$$\left. \left. + \frac{r_1 r_2}{2r_{\rm p}}(1 + \cos\psi)^2 \right] \right\}^{1/2}. \tag{19}$$

This may be integrated without problem. Parametrizing an orbit by its periapsis and eccentricity has the additional benefit of allowing easier comparison with its flat-space equivalent (Gair, Kennefick & Larson 2005).

The θ motion is usually bounded, with $\theta_0 \leqslant \theta \leqslant \pi - \theta_0$; in the event that $L_z = 0$ the particle follows a polar orbit and θ covers its full range (Wilkins 1972). The turning points are given by

$$V_\theta = Q - \cot^2\theta\, L_z^2 = 0. \tag{20}$$

If we change variable to $\zeta = \cos^2\theta$, we have a maximum value $\zeta_0 = \cos^2\theta_0$ given by

$$\zeta_0 = \frac{Q}{Q + L_z^2} = \frac{Q}{L_\infty^2}. \tag{21}$$

See Fig. 1 for a geometrical visualization. Let us now introduce a second angular variable (Drasco & Hughes 2004)

$$\zeta = \zeta_0 \cos^2\chi. \tag{22}$$

Over one 2π period of χ, θ oscillates over from its minimum value to its maximum and back. The geodesic equation for χ is

$$\rho^2 \frac{d\chi}{d\tau} = \sqrt{Q + L_z^2}, \tag{23}$$

and may be integrated simply.

3 WAVEFORM CONSTRUCTION

For given angular momenta L_z and Q, and initial starting position, we can calculate the geodesic trajectory. The orbiting body is assumed to follow this track exactly; we ignore

evolution due to the radiation of energy and angular momentum, which should be negligible for EMRBs. From this trajectory we calculate the waveform using a semirelativistic approximation (Ruffini & Sasaki 1981): we assume that the particle moves along a geodesic in the Kerr geometry, but radiates as if it were in flat spacetime. This quick-and-dirty technique is known as a numerical kludge (NK), and has been shown to approximate well results computed by more accurate methods (Babak et al. 2007). It is often compared to a bead travelling along a wire. The shape of the wire is set by the Kerr geodesic, but the bead moves along in flat space.

3.1 Kludge approximation

Numerical kludge approximations aim to encapsulate the main characteristics of a waveform by using the exact particle trajectory (ignoring inaccuracies from radiative effects and from the particle's self-force), whilst saving on computational time by using approximate waveform generation techniques.

To start, we build an equivalent flat-space trajectory from the Kerr geodesic. This is done by identifying the Boyer-Lindquist coordinates with a set of flat-space coordinates. We consider two choices here:

(i) Identify the Boyer-Lindquist coordinates with flat-space spherical polars $\{r_{\rm BL}, \theta_{\rm BL}, \phi_{\rm BL}\} \to \{r_{\rm sph}, \theta_{\rm sph}, \phi_{\rm sph}\}$, then define flat-space Cartesian coordinates (Gair et al. 2005; Babak et al. 2007)

$$\boldsymbol{x} = \begin{pmatrix} r_{\rm sph}\sin\theta_{\rm sph}\cos\phi_{\rm sph} \\ r_{\rm sph}\sin\theta_{\rm sph}\sin\phi_{\rm sph} \\ r_{\rm sph}\cos\theta_{\rm sph} \end{pmatrix}. \tag{24}$$

(ii) Identify the Boyer-Lindquist coordinates with flat-space oblate-spheroidal coordinates $\{r_{\rm BL}, \theta_{\rm BL}, \phi_{\rm BL}\} \to \{r_{\rm ob}, \theta_{\rm ob}, \phi_{\rm ob}\}$ so that the flat-space Cartesian coordinates are

$$\boldsymbol{x} = \begin{pmatrix} \sqrt{r_{\rm ob}{}^2 + a^2}\sin\theta_{\rm ob}\cos\phi_{\rm ob} \\ \sqrt{r_{\rm ob}{}^2 + a^2}\sin\theta_{\rm ob}\sin\phi_{\rm ob} \\ r_{\rm ob}\cos\theta_{\rm ob} \end{pmatrix}. \tag{25}$$

These are appealing because in the limit that $G \to 0$, where the gravitating mass goes to zero, the Kerr metric in Boyer-Lindquist coordinates reduces to the Minkowski metric in oblate-spheroidal coordinates.

In the limit of $a \to 0$, the two coincide, as they do in the limit of large r.

It must be stressed that there is no well motivated argument that either coordinate system must yield an accurate GW; their use is justified *post facto* by comparison with results obtained from more accurate, and computationally intensive, methods (Gair et al. 2005; Babak et al. 2007). The ambiguity in assigning flat-space coordinates reflects the inconsistency of the semirelativistic approximation: the geodesic trajectory was calculated for the Kerr geometry; by moving to flat spacetime we lose the reason for its existence. However, this inconsistency should not be regarded as a major problem; it is just an artifact of the basic assumption that the shape of the trajectory is important for determining the character of the radiation, but the curvature of the spacetime in the vicinity of the source is not. By

binding the particle to the exact geodesic, we ensure that the kludge waveform has spectral components at the correct frequencies, but by assuming flat spacetime for generation of GWs they shall not have the correct amplitudes.

3.2 Quadrupole-octupole formula

Now we have a flat-space particle trajectory $x_{\rm p}^\mu(\tau)$, we may apply a flat-space wave generation formula. We use the quadrupole-octupole formula to calculate the gravitational strain (Bekenstein 1973; Press 1977; Yunes et al. 2008)

$$h^{jk}(t,\boldsymbol{x}) = -\frac{2G}{c^6 r}\left(\ddot{I}^{jk} - 2n_i\dddot{S}^{ijk} + n_i\dddot{M}^{ijk}\right)_{t'=t-r/c}, \quad (26)$$

where an over-dot represents differentiation with respect to time t (and not τ), t' is the retarded time, $r = |\boldsymbol{x} - \boldsymbol{x}_{\rm p}|$ is the radial distance, $\boldsymbol{n}$ is the radial unit vector, and the mass quadrupole I^{jk}, current quadrupole S^{ijk} and mass octupole M^{ijk} are defined by

$$I^{jk}\left(t'\right) = \int x'^j x'^k T^{00}\left(t',\boldsymbol{x'}\right)\,{\rm d}^3 x'; \quad (27)$$

$$S^{ijk}\left(t'\right) = \int x'^j x'^k T^{0i}\left(t',\boldsymbol{x'}\right)\,{\rm d}^3 x'; \quad (28)$$

$$M^{ijk}\left(t'\right) = \frac{1}{c}\int x'^i x'^j x'^k T^{00}\left(t',\boldsymbol{x'}\right)\,{\rm d}^3 x'. \quad (29)$$

This is correct for a slowly moving source. It is the familiar quadrupole formula (Misner, Thorne & Wheeler 1973, section 36.10; Hobson et al. 2006, section 17.9), derived from linearized theory, plus the next order terms. For a point mass, the energy-momentum tensor $T^{\mu\nu}$ contains a δ-function which allows easy evaluation of the integrals of the various moments to give

$$I^{jk} = c^2\mu x_{\rm p}^j x_{\rm p}^k; \quad (30)$$

$$S^{ijk} = c\mu v_{\rm p}^i x_{\rm p}^j x_{\rm p}^k; \quad (31)$$

$$M^{ijk} = c\mu x_{\rm p}^i x_{\rm p}^j x_{\rm p}^k. \quad (32)$$

Since we are only interested in GWs, we use the transverse-traceless (TT) gauge. The waveform is given in the TT gauge by (Misner et al. 1973, box 35.1)

$$h_{jk}^{\rm TT} = P_j^l h_{lm} P_k^m - \frac{1}{2} P_{jk} P^{lm} h_{lm}, \quad (33)$$

where the (spatial) projection operator P_{ij} is

$$P_{ij} = \delta_{ij} - n_i n_j. \quad (34)$$

4 DETECTION WITH LISA

The classic LISA design is a three arm, space-borne laser interferometer (Bender et al. 1998; Danzmann & Rüdiger 2003). The three arms form an equilateral triangle that rotates as the system's centre of mass follows a circular, heliocentric orbit, trailing $20°$ behind the Earth. eLISA has a similar design, but only has two arms (Jennrich et al. 2011).

To describe the detector configuration, and to transform from the MBH coordinate system to those of the detector, we find it useful to define three coordinate systems: those of the BH at the GC $x_\bullet^i$; ecliptic coordinates centred at the solar system (SS) barycentre $x_\odot^i$, and coordinates that co-rotate with the detector $x_{\rm d}^i$. The MBH's coordinate system
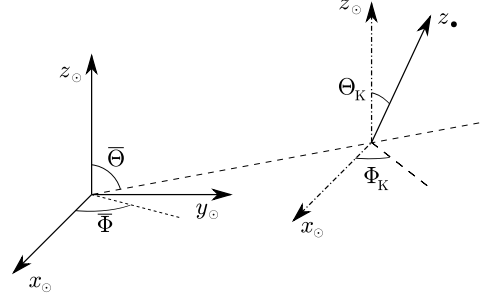


Figure 2. The relationship between the MBH's coordinate system $x_\bullet^i$ and the SS coordinate system $x_\odot^i$. The MBH's spin axis is aligned with the $z_\bullet$-axis. The orientation of the MBH's x- and y-axes is arbitrary. We choose $x_\bullet$ to be orthogonal to the direction the SS.
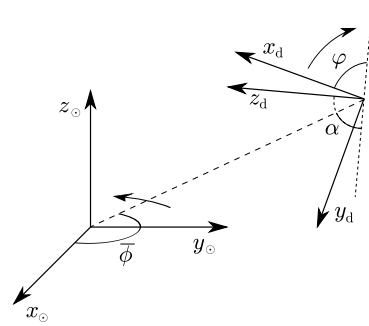
Figure 3. The relationship between the detector coordinates $x_{\rm d}^i$ and the ecliptic coordinates of the SS $x_\odot^i$ (Bender et al. 1998; Jennrich et al. 2011).

and the SS coordinate system are depicted in Fig. 2. The mission geometry for LISA/eLISA is shown in Fig. 3. We define the detector coordinates such that the detector-arms lie in the $x_{\rm d}$-$y_{\rm d}$ plane as shown in Fig. 4. The coordinate systems are related by a series of angles: $\Theta_{\rm K}$ and $\Phi_{\rm K}$ give the orientation of the MBH's spin axis relative to the SS's coordinates. $\overline{\Theta}$ and $\overline{\Phi}$ give the position of the GC in ecliptic coordinates. $\overline{\phi}$ gives the detector's orbital phase and φ gives the rotational phase of the detector arms. Both of these vary
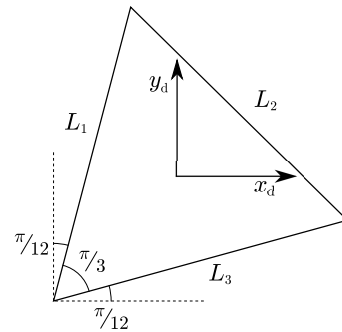
Figure 4. The alignment of the three detector arms, with lengths L_1, L_2 and L_3, within the $x_{\rm d}$-$y_{\rm d}$ plane (Cutler 1998). The origin of the detector coordinates coincides with the centre of mass of the constellation of satellites.

linearly with time

$$\overline{\phi}(t) = \omega_\oplus t + \overline{\phi}_0; \quad \varphi(t) = -\omega_\oplus t + \varphi_0; \tag{35}$$

where $\omega_\oplus$ corresponds to one rotation per year. Finally, $\alpha = 60°$ is the inclination of the detector plane. We have computed the waveforms in the MBH's coordinates, however it is simplest to describe the measured signal using the detector's coordinates.

The strains measured in the three arms can be combined such that LISA behaves as a pair of 90° interferometers at 45° to each other, with signals scaled by $\sqrt{3}/2$ (Cutler 1998). We denote the two detectors as I and II. If we label the change in the three arms' lengths caused by GWs δL_1, δL_2 and δL_3, and use L for the unperturbed length, then detector I measures strain

$$h_\mathrm{I}(t) = \frac{\delta L_1 - \delta L_2}{L} = \frac{\sqrt{3}}{2}\left(\frac{1}{2}h_\mathrm{d}^{xx} - \frac{1}{2}h_\mathrm{d}^{yy}\right), \tag{36}$$

and detector II measures

$$h_\mathrm{II}(t) = \frac{\delta L_1 + \delta L_2 - 2\delta L_3}{\sqrt{3}L} = \frac{\sqrt{3}}{2}\left(\frac{1}{2}h_\mathrm{d}^{xy} + \frac{1}{2}h_\mathrm{d}^{yx}\right). \tag{37}$$

We use vector notation $\boldsymbol{h}(t) = (h_\mathrm{I}(t), h_\mathrm{II}(t)) = \{h_A(t)\}$ to represent signals from both detectors.

The final consideration for calculating the signal measured by LISA is the time of arrival of the signal: LISA's orbital position changes with time. Fortunately over the timescales of interest for EMRBs, these changes are small. We assume that the position of the SS barycentre relative to the GC is constant: it is defined by the distance R_0 and the angles $\overline{\Theta}$ and $\overline{\Phi}$. The time of arrival at the SS barycentre $t_\odot$ is then the retarded time; the time of detection t_d to lowest order is

$$t_\mathrm{d} \simeq t_\odot - t_\mathrm{AU} \cos\left[\overline{\phi}(t_\odot) - \overline{\Phi}\right]\sin\overline{\Theta}, \tag{38}$$

where t_AU is the light travel-time for the detector's orbital radius. The time t_d is required for $\phi(t)$ and $\varphi(t)$.

5   SIGNAL ANALYSIS

5.1   Frequency domain formalism

Having constructed the GW $\boldsymbol{h}(t)$ that shall be incident upon the detector, we may now consider how to analyse the waveform and extract the information it contains. We begin with a brief overview of the basic components of signal analysis used for GWs, with application to LISA in particular. This fixes notation. A more complete discussion can be found in Finn (1992), and Cutler & Flanagan (1994). Adaption for eLISA requires a substitution of the noise distribution, and the removal of the sum over detectors, since it will only have one.

The measured strain $\boldsymbol{s}(t)$ is the combination of the signal and the detector noise

$$\boldsymbol{s}(t) = \boldsymbol{h}(t) + \boldsymbol{n}(t); \tag{39}$$

we assume that the noise $n_A(t)$ is stationary and Gaussian. It is more convenient to work with the Fourier transform

$$\tilde{g}(f) = \mathscr{F}\{g(t)\} = \int_{-\infty}^{\infty} g(t)e^{2\pi i f t}\,\mathrm{d}t. \tag{40}$$

For a Gaussian noise signal $n_A(t)$, each Fourier component $\tilde{n}_A(f)$ has a Gaussian probability distribution; the assumption of stationarity means that different Fourier components are uncorrelated, thus (Cutler & Flanagan 1994)

$$\langle \tilde{n}_A(f)\tilde{n}_B^*(f')\rangle_n = \frac{1}{2}\delta(f - f')S_{AB}(f), \tag{41}$$

where $\langle\ldots\rangle_n$ denotes the expectation value over the noise distribution, and $S_{AB}(f)$ is the (single-sided) noise spectral density. For simplicity, we may assume that the noise in the two detectors is uncorrelated, but share the same characterisation so that (Cutler 1998)

$$S_{AB}(f) = S_n(f)\delta_{AB}. \tag{42}$$

The functional form of the noise spectral density $S_n(f)$ for LISA is discussed in Sec. 5.2.

The properties of the noise allow us to define a natural inner product and associated distance on the space of signals (Cutler & Flanagan 1994)

$$(\boldsymbol{g}|\boldsymbol{k}) = 2\int_0^\infty \frac{\tilde{g}_A^*(f)\tilde{k}_A(f) + \tilde{g}_A(f)\tilde{k}_A^*(f)}{S_n(f)}\,\mathrm{d}f. \tag{43}$$

Using this definition, the signal-to-noise ratio is approximately

$$\rho[\boldsymbol{h}] = (\boldsymbol{h}|\boldsymbol{h})^{1/2}. \tag{44}$$

The probability of a particular realization of noise $\boldsymbol{n}(t) = \boldsymbol{n}_0(t)$ is

$$p(\boldsymbol{n}(t) = \boldsymbol{n}_0(t)) \propto \exp\left[-\frac{1}{2}(\boldsymbol{n}_0|\boldsymbol{n}_0)\right]. \tag{45}$$

If the incident waveform is $\boldsymbol{h}(t)$, the probability of measuring signal $\boldsymbol{s}(t)$ is

$$p(\boldsymbol{s}(t)|\boldsymbol{h}(t)) \propto \exp\left[-\frac{1}{2}(\boldsymbol{s} - \boldsymbol{h}|\boldsymbol{s} - \boldsymbol{h})\right]. \tag{46}$$

5.2   Noise curve

LISA's noise has two sources: instrumental noise and confusion noise, primarily from white dwarf binaries. The latter may be divided into contributions from galactic and extragalactic binaries. In this work we use the noise model of Barack & Cutler (2004). The shape of the noise curve can be seen in Fig. 5. The instrumental noise dominates at both high and low frequencies. The confusion noise is important at intermediate frequencies, and is responsible for the cusp around $f = 10^{-3}$ Hz. eLISA shares the same sources of noise, but is less affected by confusion. Its sensitivity regime is shifted to higher frequencies because of a shorter arm length.

5.3   Window functions

There is one remaining complication regarding signal analysis: since we are Fourier transforming a finite signal we encounter spectral leakage; a contribution from large amplitude spectral components leaks into surrounding components (sidelobes), obscuring and distorting the spectrum at these frequencies (Harris 1978). This is an inherent problem with finite signals; it shall be as much of a problem when analysing signals from an actual mission as it is computing waveforms here. To mitigate, but unfortunately not eliminate, these effects, the time-domain signal can be multiplied
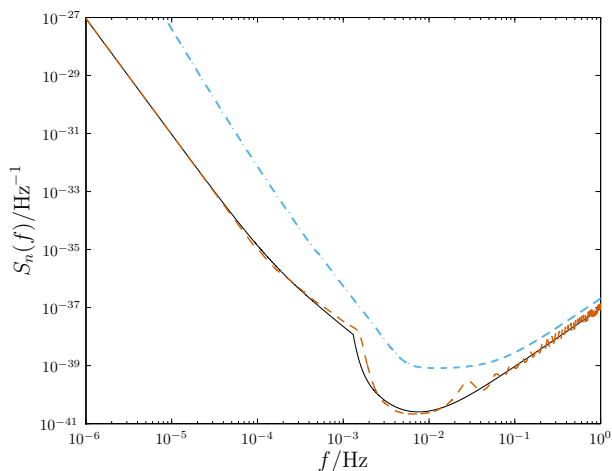
Figure 5. The detector noise curves. The solid line indicates the analytic approximation of Barack & Cutler (2004) used in this work. For comparison, the dashed line is from the online LISA sensitivity curve generator (http://www.srl.caltech.edu/~shane/sensitivity/; Larson, Hiscock & Hellings 2000; Larson, Hellings & Hiscock 2002). For parabolic encounters we are most interested in the low-frequency region where the two curves are the same. The dot-dashed line shows the eLISA noise curve.

by a window function. These are discussed in detail in Appendix A. We have adopted the Nuttall four-term window with continuous first derivative (Nuttall 1981) for the results presented here.

6 WAVEFORMS AND DETECTABILITY

6.1 Model parameters

The shape of the waveform depends on a number of parameters: those defining the MBH; those defining the companion object on its orbit, and those defining the LISA detector. Let us define $\boldsymbol{\lambda} = \left\{ \lambda^1, \lambda^2, \ldots, \lambda^Z \right\}$ as the set of Z parameters which specify the GW. For our model, the input parameters are:

(1) The MBH's mass $M_\bullet$. This is currently well constrained by the observation of stellar orbits about Sgr A* (Ghez et al. 2008; Gillessen et al. 2009), with the best estimate being $M_\bullet = (4.31 \pm 0.36) \times 10^6 M_\odot$. However this depends upon the galactic centre distance R_0 being accurately known. If the uncertainty in this is included $M_\bullet = (3.95 \pm 0.06|_{\text{stat}} \pm 0.18|_{R_0, \text{stat}} \pm 0.31|_{R_0, \text{sys}}) \times 10^6 M_\odot (R_0/8 \text{ kpc})^{2.19}$, where the errors are statistical, independent of R_0; statistical from the determination of R_0, and systematic from R_0 respectively.

(2) The spin parameter a_*. Naively this could be anywhere in the range $|a_*| < 1$; however it is possible to place an upper bound by contemplating spin-up mechanisms. Considering the torque from radiation emitted by an accretion disc, and swallowed by the BH, it can be shown that $|a_*| \lesssim 0.998$ (Thorne 1974). Magnetohydrodynamical simulations of accretion discs produce a smaller maximum value of $|a_*| \sim 0.95$ (Gammie et al. 2004). The actual spin value

could be much lower than this upper bound depending upon the MBH's evolution (as discussed in Sec. 1).

(3,4) The orientation angles for the black hole spin Θ_{K} and Φ_{K}.

(5) The ratio of the SS-GC distance R_0 and the compact object mass μ, which we denote as $\zeta = R_0/\mu$. These two parameters are degenerate, ζ scales the amplitude of the waveform, so they cannot be inferred separately. The distance, like $M_\bullet$, is constrained by stellar orbits, the best estimate being (Gillessen et al. 2009) $R_0 = 8.33 \pm 0.35$ kpc. The mass of the orbiting particle depends upon the type of object: whether it is an MS star, WD, NS or BH. Since we shall not know the compact object mass precisely, we shall not be able to infer anything more about the distance to the GC.

(6, 7) The angular momentum of the compact object. This can be described using either $\{L_z, Q\}$ or $\{L_\infty, \iota\}$. We employ the latter, as the total angular momentum and inclination are less tightly correlated. Assuming spherical symmetry, we expect $\cos \iota$ to be uniformly distributed.

(8–10) A set of coordinates to specify the trajectory. These could be positions at an arbitrary time. We use the angular phases at periapse, ϕ_{p} and χ_{p} (which determines θ_{p}), as well as the time of periapse t_{p}.

(11, 12) The coordinates of the MBH from the SS barycentre $\overline{\Theta}$ and $\overline{\Phi}$. These may be taken as the coordinates of Sgr A*, as the radio source is expected to be within ten Schwarzschild radii of the MBH (Reid et al. 2003; Doeleman et al. 2008). At the epoch J2000.0 $\overline{\Theta} = 95.607669°$, $\overline{\Phi} = 266.851760°$ (Reid et al. 1999; Yusef-Zadeh et al. 1999). They change with time due to the rotation of the SS about the GC, the proper motion is about 6 mas yr^{-1}, mostly in the plane of the galaxy (Reid et al. 1999; Backer & Sramek 1999; Reid et al. 2003). The position is already determined to high accuracy: an EMRB can only give weak constraints on source position. Therefore we take it as known and shall not try to infer it.

(13, 14) The orbital position of the LISA satellites given by $\overline{\phi}$ and φ. We assume that the initial positions are chosen such that $\overline{\phi} = 0$ when $\varphi = 0$ (Cutler 1998); this choice does not qualitatively influence our results. The orbital position should be known, so this need not be inferred.

We therefore have an 14 dimensional parameter space, of which we are interested in inferring $d = 10$ parameters.
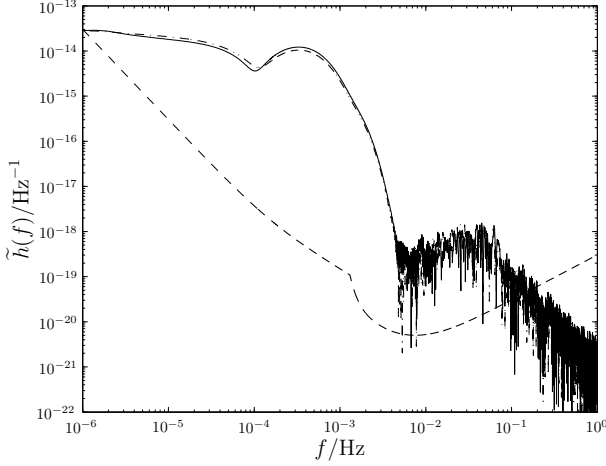
6.2 Waveforms

Figure 6.2 show example waveforms to demonstrate some of the possible variations in the signal. All these assume the standard mass and position for the MBH as well as a $\mu = 10 M_\odot$ orbiting CO; other orbital parameters are specified in the captions. Radii are given in terms of the gravitational radius $r_{\text{g}} = GM_\bullet/c^2$.
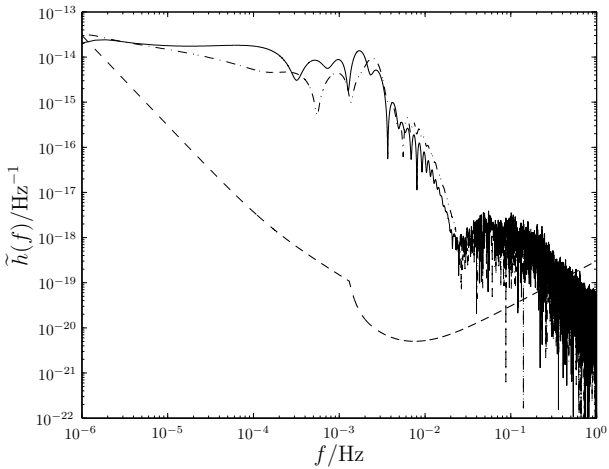
The plotted waveforms use the spherical polar coordinate system for the NK. Using oblate-spheroidal coordinates makes a small difference: on the scale shown here the only discernible difference would be in Fig. 6(c); the maximum difference in the waveform (outside the high-frequency tail) is $\sim 10\%$. In the other cases the difference is entirely negligible (except in the high-frequency tail, which is not of physi-
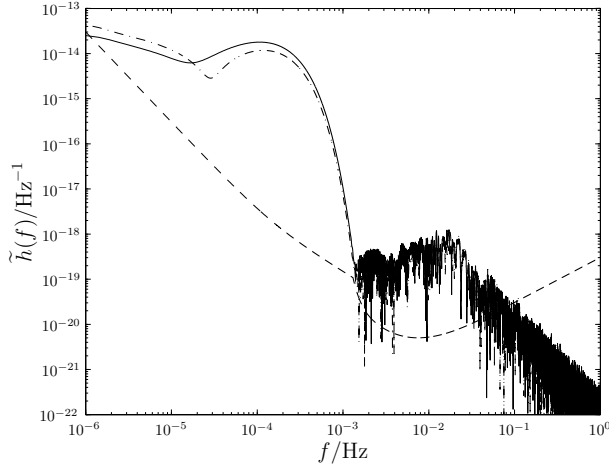
(a) Waveform for $a_* \simeq 0.12$, $r_\mathrm{p} \simeq 15.6 r_\mathrm{g}$ and $\iota \simeq 2.1$. The SNR for the spherical polar kludge waveform (plotted) is $\rho[\boldsymbol{h}_\mathrm{sph}] \simeq 451$, for the oblate-spheroidal kludge it is $\rho[\boldsymbol{h}_\mathrm{ob}] \simeq 451$ (agreement to 0.01%).

(b) Waveform for $a_* \simeq 0.48$, $r_\mathrm{p} \simeq 8.8 r_\mathrm{g}$ and $\iota \simeq 2.0$. The SNR for the spherical polar kludge waveform (plotted) is $\rho[\boldsymbol{h}_\mathrm{sph}] \simeq 2300$, for the oblate-spheroidal kludge it is $\rho[\boldsymbol{h}_\mathrm{ob}] \simeq 2310$.

(c) Waveform for $a_* \simeq 0.74$, $r_\mathrm{p} \simeq 3.2 r_\mathrm{g}$ and $\iota \simeq 1.2$. The SNR for the spherical polar kludge waveform (plotted) is $\rho[\boldsymbol{h}_\mathrm{sph}] \simeq 70600$, for the oblate-spheroidal kludge it is $\rho[\boldsymbol{h}_\mathrm{ob}] \simeq 74900$.

Figure 6. Example burst waveforms from the galactic centre. The strain $\widetilde{h}_\mathrm{I}(f)$ is indicated by the solid line, $\widetilde{h}_\mathrm{II}(f)$ by the dot-dashed line, and the noise curve by the dashed line. The kludge has been formulated using spherical coordinates coordinates.
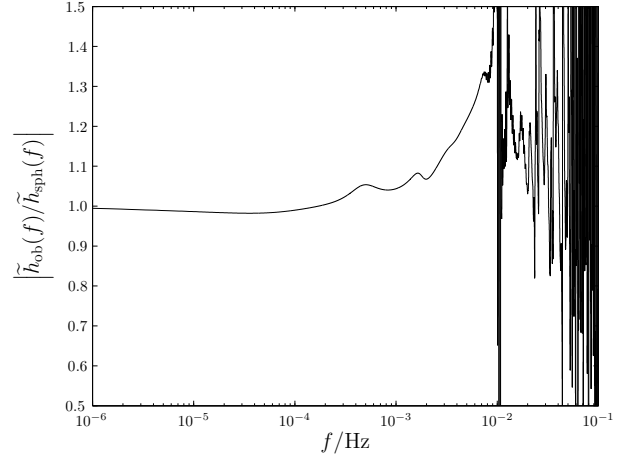
Figure 7. Comparison of waveforms generated using oblate-spheroidal and spherical polar coordinates for the numerical kludge. Both $\widetilde{h}_\mathrm{I}(f)$ and $\widetilde{h}_\mathrm{II}(f)$ show the same behaviour. The effects of numerical noise are seen at high-frequencies.

cal significance). This behaviour is typical, for the closest orbits, with the most extreme spin parameters, the maximum difference in the waveforms may be $\sim 30\%$, but only across a small region. The difference from the coordinate systems is only apparent for orbits with very small periapses when the MBH has a high spin. The difference is largely confined to the higher frequency components, which are most sensitive to the parts of the trajectory closer to the MBH: the change in flat-space radius for the same Boyer-Lindquist radial coordinate causes a slight shift in the shape of the spectrum. Enforcing the same flat-space periapse radius gives worse agreement across the spectrum.

Since the deviation in the two waveforms is only apparent for small periapses, when the kludge approximation is least applicable, we conclude that the choice of coordinates is unimportant. The potential error of order 10% is less than that inherent in the NK approximation (see Sec. 7). Without an accurate waveform template to compare against, we do not know if there is a preferable choice of coordinates. We adopt spherical coordinates for the rest of this work.

6.3 Signal-to-noise ratios

The detectability of a burst depends upon its SNR. To characterise the variation of ρ we considered a range of orbits. In each case the MBH was assumed to have a mass of $M_\bullet = 4.31 \times 10^6 M_\odot$, and to be at the J2000.0 coordinates and a distance of $R_0 = 8.33$ kpc.

These bursts were calculated for a $1 M_\odot$ CO. From (26), the amplitude of the waveform is proportional to the CO mass μ and so ρ is also proportional to μ; a $10 M_\odot$ object would be ten times louder on the same orbit. To make results mass independent, we shall work in terms of a mass-normalised SNR

$$\hat{\rho}[\boldsymbol{h}] = \frac{\rho[\boldsymbol{h}]}{\mu}. \tag{47}$$

The spin of the MBH and the orbital inclination were randomly chosen, and the periapse distance was set so that the distribution would be uniform in log-space (up to the point of the inner-most stable orbit). For each set of these
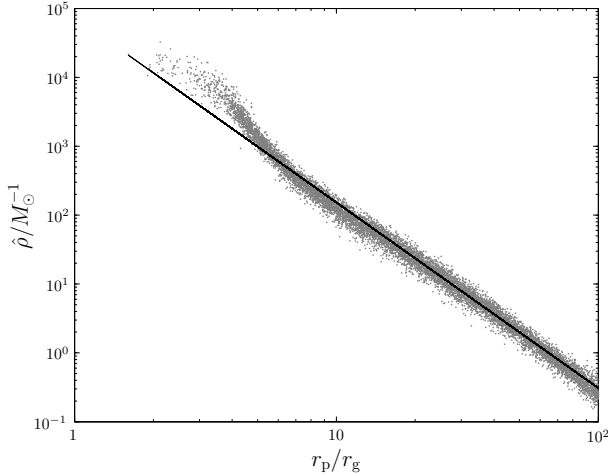
Figure 8. Mass-normalised SNR as a function of periapse radius. The plotted points are the values obtained by averaging over each set of intrinsic parameters. The best fit line is $\log(\hat{\rho}/M_\odot^{-1}) = -2.69 \log(r_{\rm p}/r_{\rm g}) + 4.88$. This is fitted to orbits with $r_{\rm p} > 13.0 r_{\rm g}$ and has a reduced chi-squared value of $\chi^2/\nu = 1.73$.

extrinsic parameters, the periapse position, orientation of the MBH, and orbital position of detector were varied: five random combinations of these intrinsic parameters (each being drawn from a separate uniform distribution) were used for at each point.

We take the mean of $\ln \rho$ for each set of randomised intrinsic parameters (starting position, MBH orientation and detector orientation).[4]

There exists a correlation between the periapse radius and SNR, as shown in Fig. 8. Closer orbits produce louder bursts. To reflect this relationship, we have fitted a simple fiducial power law, as indicated by the straight line. This was done by maximising the likelihood, assuming that $\ln \rho$ has a Gaussian distribution with standard deviation derived from the scatter of from variation in the intrinsic parameters. The power law appears to be a good fit only for orbits with larger periapses. The shape of the curve is predominately determined by the shape of the noise curve. The change in the trend reflects the change as we go from approximately power law behaviour into the bucket of the curve. Hence, we fit a power law to orbits with a characteristic frequency of $f_* = \sqrt{GM_\bullet/r_{\rm p}} < 1 \times 10^{-3}$ Hz, so as to avoid spilling over into the bucket.[5] Changing the cut-off within a plausible region alters the fit coefficients by around 0.1.

The SNR shows no clear correlation with the other parameters (excluding the mass μ). However, the SNR is sensitive to the intrinsic parameters, in particular the initial position (as this determines the subsequent trajectory), and may vary by an order of magnitude.

Setting a detection threshold of $\rho = 10$, a $1 M_\odot$ ($10 M_\odot$)

---

[4] The logarithm is a better quantity to work with since the SNR is a positive-definite quantity that may be distributed over a range of magnitudes (MacKay 2003, sections 22.1, 23.3). Using median values yields results that are quantitatively similar.

[5] The power law exponent -2.7 is inconsistent with $-13/4$ as predicted by the approximate model of Hopman et al. (2007).

object would be expected to be detectable if the the periapse distance is less than $27 r_{\rm g}$ ($65 r_{\rm g}$).

7 ENERGY SPECTRA

To check that the NK waveforms are sensible, we may compare the energy spectra calculated from these with those obtained from the classic treatment of Peters & Mathews (1963), and Peters (1964). This calculates GW emission for Keplerian orbits in flat spacetime, assuming only quadrupole radiation. The spectrum produced should be similar to that obtained from the NK in weak fields, that is for orbits with a large periapsis; however, we do not expect an exact match because of the differing input physics and varying approximations.

In addition to using the energy spectrum, we can also use the total energy flux to check the NK waveforms. The total flux contains less information than the spectrum; however, results have been calculated for parabolic orbits in Schwarzschild spacetime using time-domain black hole perturbation theory (Martel 2004). These should be more accurate than results calculated using the Peters and Mathews formalism.

We do not intend to use the kludge waveforms to calculate an accurate energy flux: this would be inconsistent as we assume that the orbits do not evolve with time. We only calculate the energy flux as a sanity check, to confirm that the kludge approximation is consistent with other approaches.

7.1 Kludge spectrum

A gravitational wave in the TT gauge has an effective energy-momentum tensor (Misner et al. 1973, section 35.15)

$$T_{\mu\nu} = \frac{c^4}{32\pi G} \left\langle \partial_\mu h_{ij} \partial_\nu h^{ij} \right\rangle, \tag{48}$$

where $\langle \ldots \rangle$ indicates averaging over several wavelengths or periods. The flux of energy through a sphere of radius $r = R$ is

$$\frac{dE}{dt} = \frac{c^3}{32\pi G} R^2 \int d\Omega \left\langle \frac{dh_{ij}}{dt} \frac{dh^{ij}}{dt} \right\rangle, \tag{49}$$

with $\int d\Omega$ representing integration over all solid angles. From (26) we see that the waves have a $1/r$ dependence; if we define

$$h_{ij} = \frac{H_{ij}}{r}, \tag{50}$$

we see that, using (26), the flux is independent of R, as required for energy conservation, and

$$\frac{dE}{dt} = \frac{c^3}{32\pi G} \int d\Omega \left\langle \frac{dH_{ij}}{dt} \frac{dH^{ij}}{dt} \right\rangle. \tag{51}$$

If we now integrate to find the total energy emitted we obtain

$$E = \frac{c^3}{32\pi G} \int d\Omega \int_{-\infty}^{\infty} dt \, \frac{dH_{ij}}{dt} \frac{dH^{ij}}{dt}. \tag{52}$$

Since we are considering all time, the localization of the energy is no longer of importance and it is unnecessary to

average over several periods. Switching to Fourier representation $\widetilde{H}_{ij}(f) = \mathscr{F}\{H_{ij}(t)\}$,

$$E = \frac{\pi c^3}{4G} \int \mathrm{d}\Omega \int_0^\infty \mathrm{d}f\, f^2 \widetilde{H}^{ij}(f)\widetilde{H}_{ij}^*(f), \qquad (53)$$

using the fact that the signal is real so $\widetilde{H}_{ij}^*(f) = \widetilde{H}_{ij}(-f)$. From this we identify the energy spectrum as

$$\frac{\mathrm{d}E}{\mathrm{d}f} = \frac{\pi c^3}{4G} \int \mathrm{d}\Omega\, f^2 \widetilde{H}^{ij}(f)\widetilde{H}_{ij}^*(f). \qquad (54)$$

7.2 Peters and Mathews spectrum

To calculate the Peters and Mathews energy spectrum for a parabolic orbit, we use the limiting result of Turner (1977)

$$\frac{\mathrm{d}E}{\mathrm{d}f} = \frac{4\pi^2}{5}\frac{G^3}{c^5}\frac{M_\bullet^2\mu^2}{r_\mathrm{p}^2}\left\{\left[\frac{8f^2}{f_\mathrm{c}^2}B\left(\frac{f}{f_\mathrm{c}}\right) - \frac{2f}{f_\mathrm{c}}A\left(\frac{f}{f_\mathrm{c}}\right)\right]^2 \right.$$
$$\left. + \left(\frac{128f^4}{f_\mathrm{c}^4} + \frac{4f^2}{3f_\mathrm{c}^2}\right)\left[A\left(\frac{f}{f_\mathrm{c}}\right)\right]^2\right\}, \qquad (55)$$

where f_c is the orbital frequency of a circular orbit of radius equal to r_p,

$$f_\mathrm{c} = \frac{1}{2\pi}\sqrt{\frac{G(M_\bullet + \mu)}{r_\mathrm{p}^3}}, \qquad (56)$$

and functions $A(x)$ and $B(x)$ are defined in terms of Bessel functions. Their precise forms are (Berry & Gair 2010)

$$A(x) = \frac{1}{\pi}\sqrt{\frac{2}{3}}K_{1/3}\left(\frac{2^{3/2}x}{3}\right); \qquad (57)$$

$$B(x) = \frac{1}{\sqrt{3}\pi}\left[K_{-2/3}\left(\frac{2^{3/2}x}{3}\right) + K_{4/3}\left(\frac{2^{3/2}x}{3}\right)\right.$$
$$\left. - \frac{1}{\sqrt{2}x}K_{1/3}\left(\frac{2^{3/2}x}{3}\right)\right], \qquad (58)$$

where $K_\nu(z)$ is a modified Bessel function of the second kind. This result should be accurate to $\sim 10\%$ for orbits with periapse radii larger than $\sim 20r_\mathrm{g}$ (Berry & Gair 2010).

7.3 Comparison

Two energy spectra are plotted in Fig. 9 for orbits with periapses of $r_\mathrm{p} = 15.0r_\mathrm{g}$, $30.0r_\mathrm{g}$ and $60.0r_\mathrm{g}$. The two spectra appear to be in good agreement, showing the same general shape in the weak-field limit. The NK spectrum is more tightly peaked, but is always within a factor of 2 at the apex. The peak of the spectrum is shifted to a marginally higher frequency in the NK spectrum because of the contribution from the current quadrupole and mass octupole terms.

Comparing the total energy fluxes, ratios of the various energies are plotted in Fig. 10. We introduce an additional energy here, the quadrupole NK energy $E_{\mathrm{NK(Q)}}$. This allows easier comparison with the Peters and Mathews energy which includes only quadrupole radiation. It can be calculated in three ways:

(i) Inserting the waveform $\widetilde{h}(f)$ generated including only the mass quadrupole term in (26) into (53) and integrating. This is equivalent to the method used to calculate E_{NK}.

(ii) Numerically integrating the quadrupole GW luminosity (Misner et al. 1973, section 36.7; Hobson et al. 2006, section 18.7)

$$E = \frac{G}{5c^9}\int \dddot{\mathcal{I}}_{ij}\dddot{\mathcal{I}}^{ij}\,\mathrm{d}t, \qquad (59)$$

where $\mathcal{I}_{ij} = I_{ij} - (1/3)I\delta_{ij}$ is the reduced mass quadrupole tensor. We can obtain this from (52), by integrating over all angles when the waveform only contains the mass quadrupole component. This has the advantage of avoiding the effects of spectral leakage or the influence of window functions.
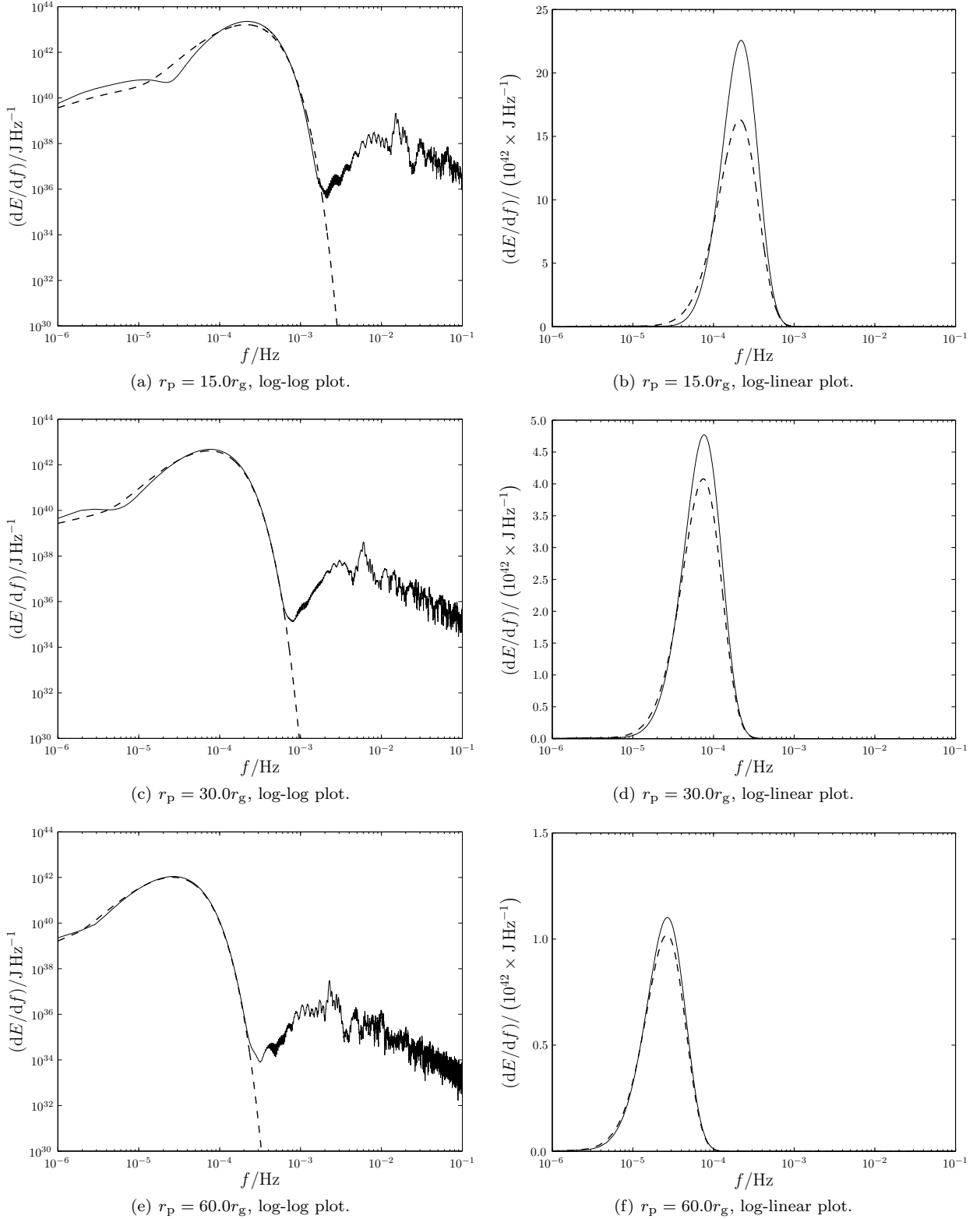
(iii) Using the analytic expressions for the integral (59) given in appendix A of Gair et al. (2005).

All three agree to within computational error. No difference is visible on the scale plotted in Fig. 10. This demonstrates the validity of the code, and shows that the use of a window function does not significantly distort the waveform.

The ratios all tend towards one in the weak field, as required, but differences become more pronounced in the strong field. The NK energy is larger than the Peters and Mathews result E_{PM}. This behaviour has been seen before for high eccentricity orbits about a non-spinning BH (Gair et al. 2005). It may be explained by considering the total path length for the different orbits: the Peters and Mathews spectrum assumes a Keplerian orbit, the orbit in Kerr geometry rotates more than this. The greater path length leads to increased emission of gravitational waves and a larger energy flux (Berry & Gair 2010). Our bead must travel further along its wire. A good proxy for the path length is the angle of rotation $\Delta\phi$; this is 2π for a Keplerian orbit, in Kerr the angle should be 2π in the limit of an infinite periapsis, whereas for a periapsis small enough that the orbit shows zoom-whirl behaviour, the total angle may be many times 2π. There is a reasonable correlation between the amount of rotation $2\pi/\Delta\phi$ and the ratio of energies.

Error in the NK energy compared with the time-domain black hole perturbation theory results of Martel comes from two sources: the neglecting of higher order multipole contributions and the ignoring of background curvature. The contribution of the former can be estimated by looking at the difference in the NK energy by including the current quadrupole and mass octupole terms. From Fig. 10 we see that these terms give a negligible contribution in the weak field, but the difference is $\sim 20\%$ in the strong field. This explains why the Martel energy E_{M} is greater in the strong field, as it includes contributions from all multipoles. Neglecting the background curvature increases the NK energy relative to E_{M}. This partially cancels out the error introduced by not including higher order terms: this accidentally leads to $E_{\mathrm{NK(Q)}}$ being more accurate than E_{NK} for $r_\mathrm{p} \gtrsim 10r_\mathrm{g}$ (Tanaka et al. 1993).

From the level of agreement we may be confident that the NK waveforms are a reasonable approximation. The difference in energy flux is only greater than 10% for very strong fields $r_\mathrm{p} \simeq 4r_\mathrm{g}$; since this is dependent on the square of the waveform, typical accuracy in the waveform may be $\sim 5\%$ (Gair et al. 2005; Tanaka et al. 1993). This is more significant than the variation in waveforms we generally found using the two alternative coordinate systems for the NK (in this case the two coincide because $a_* = 0$).

(a) $r_\mathrm{p} = 15.0 r_\mathrm{g}$, log-log plot.

(b) $r_\mathrm{p} = 15.0 r_\mathrm{g}$, log-linear plot.

(c) $r_\mathrm{p} = 30.0 r_\mathrm{g}$, log-log plot.

(d) $r_\mathrm{p} = 30.0 r_\mathrm{g}$, log-linear plot.

(e) $r_\mathrm{p} = 60.0 r_\mathrm{g}$, log-log plot.

(f) $r_\mathrm{p} = 60.0 r_\mathrm{g}$, log-linear plot.

Figure 9. Energy spectra for a parabolic orbit of a $\mu = 10 M_\odot$ object about a Schwarzschild BH with $M_\bullet = 4.31 \times 10^6 M_\odot$. The spectra calculated from the NK waveform is shown by the solid line and the Peters and Mathews flux is indicated by the dashed line. The NK waveform includes octupole contributions. The high frequency tail is the result of spectral leakage.

(a) Versus periapsis

(b) Versus amount of rotation
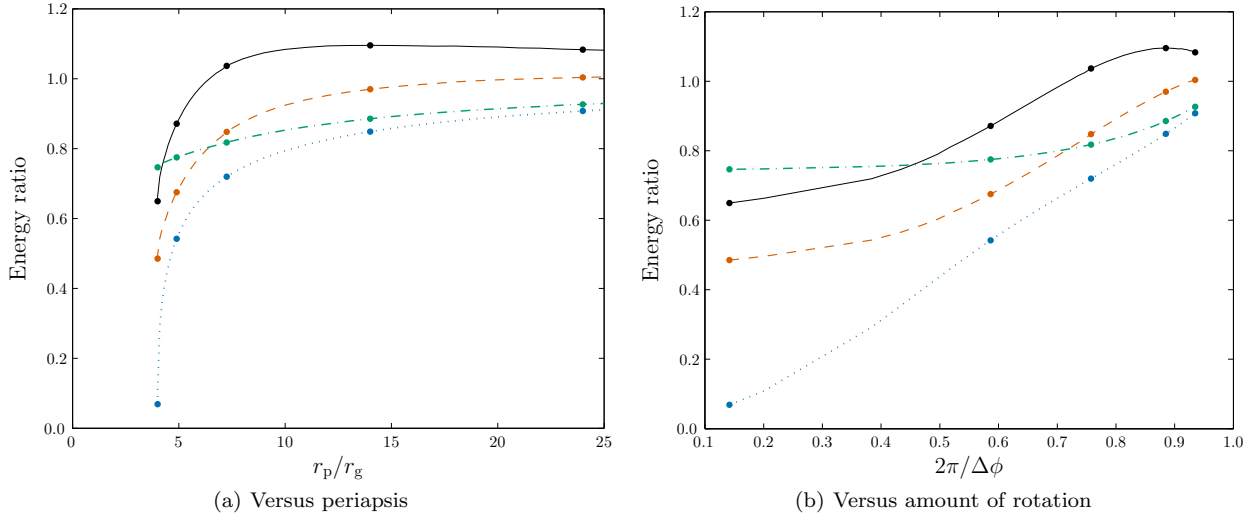
Figure 10. Ratios of energies as a function of periapsis r_{p} and 2π divided by the total angle of rotation in one orbit $\Delta\phi$ ($2\pi/\Delta\phi = 1$ for a Keplerian orbit). The solid line shows the ratio of the numerical kludge and Martel energies $E_{\mathrm{NK}}/E_{\mathrm{M}}$; the dashed line shows the ratio of the NK energy calculated using only the mass quadrupole term and the Martel energy $E_{\mathrm{NK(Q)}}/E_{\mathrm{M}}$; the dot-dashed line shows the ratio of the quadrupole and quadrupole-octupole NK energies $E_{\mathrm{NK(Q)}}/E_{\mathrm{NK}}$, and the dotted line shows the ratio of the Peters and Mathews and quadrupole NK energies $E_{\mathrm{PM}}/E_{\mathrm{NK(Q)}}$. The spots show the mapping between the two abscissa scales. Compare with figure 4 of Gair et al. (2005).

8 PARAMETER ESTIMATION

Having detected a GW signal $\boldsymbol{s}(t)$, we are interested in what we can learn about the source. We have an inference problem that can be solved by appropriate application of Bayes' Theorem (Jaynes 2003, chapter 4): the probability distribution for our parameters given that we have detected the signal $\boldsymbol{s}(t)$ is given by the posterior

$$p(\boldsymbol{\lambda}|\boldsymbol{s}(t)) = \frac{p(\boldsymbol{s}(t)|\boldsymbol{\lambda})p(\boldsymbol{\lambda})}{p(\boldsymbol{s}(t))}. \qquad (60)$$

Here $p(\boldsymbol{s}(t)|\boldsymbol{\lambda})$ is the likelihood of the parameters, $p(\boldsymbol{\lambda})$ is the prior probability distribution for the parameters, and $p(\boldsymbol{s}(t)) = \int p(\boldsymbol{s}(t)|\boldsymbol{\lambda})\,\mathrm{d}^N\lambda$ is, for our purposes, a normalising constant and may be ignored. The likelihood function depends upon the realization of noise. A particular set of parameters $\boldsymbol{\lambda}_0$ defines a waveform $\boldsymbol{h}_0(t) = \boldsymbol{h}(t;\boldsymbol{\lambda}_0)$, the probability that we observe signal $\boldsymbol{s}(t)$ for this GW is given by (46), so the likelihood is

$$p(\boldsymbol{s}(t)|\boldsymbol{\lambda}_0) \propto \exp\left[-\frac{1}{2}\left(\boldsymbol{s} - \boldsymbol{h}_0|\boldsymbol{s} - \boldsymbol{h}_0\right)\right]. \qquad (61)$$

If we were to define this as a probability distribution for the parameters $\boldsymbol{\lambda}$, then the modal values should be the maximum-likelihood parameters $\boldsymbol{\lambda}_{\mathrm{ML}}$. The waveform $\boldsymbol{h}(t;\boldsymbol{\lambda}_{\mathrm{ML}})$ is the signal closest to $\boldsymbol{s}(t)$ in the space of all signals, where distance is defined using the inner product (43) (Cutler & Flanagan 1994).

8.1 Fisher matrices

In the limit of a high SNR, we may approximate this as (Vallisneri 2008)

$$p(\boldsymbol{s}(t)|\boldsymbol{\lambda}_0) \propto \exp\left[-\frac{1}{2}\left(\partial_a\boldsymbol{h}|\partial_b\boldsymbol{h}\right)(\lambda^a - \langle\lambda^a\rangle_\ell)\left(\lambda^b - \left\langle\lambda^b\right\rangle_\ell\right)\right],$$

$$(62)$$

where the mean is defined as

$$\langle\lambda^a\rangle_\ell = \frac{\int \lambda^a p(\boldsymbol{s}(t)|\boldsymbol{\lambda})\,\mathrm{d}^N\lambda}{\int p(\boldsymbol{s}(t)|\boldsymbol{\lambda})\,\mathrm{d}^N\lambda}. \qquad (63)$$

Using the high SNR limit, this is the maximum-likelihood value $\langle\lambda^a\rangle_\ell = \lambda_{\mathrm{ML}}^a$. The quantity

$$\Gamma_{ab} = (\partial_a\boldsymbol{h}|\partial_b\boldsymbol{h}) \qquad (64)$$

is the Fisher information matrix. It controls the variance of the likelihood distribution.

The form of the posterior distribution depends upon the nature of the prior information. If we have an uninformative prior, such that $p(\boldsymbol{\lambda})$ is a constant, then the posterior distribution is determined by the likelihood. In the high SNR limit, we obtain a Gaussian with variance-covariance matrix

$$\boldsymbol{\Sigma} = \boldsymbol{\Gamma}^{-1}. \qquad (65)$$

The Fisher information matrix gives the uncertainty associated with the estimated parameter values, in this case the maximum-likelihood values.

If the prior were to restrict the allowed range for a parameter, for example, as is the case for the spin a_*, then the posterior is a truncated Gaussian, and $\boldsymbol{\Gamma}^{-1}$ may no longer represent the variance-covariance.

If the prior were approximately Gaussian with variance-covariance matrix $\boldsymbol{\Sigma}_0$, then the posterior is also Gaussian.[6] The posterior variance-covariance is (Cutler & Flanagan 1994; Vallisneri 2008)

$$\boldsymbol{\Sigma} = \left(\boldsymbol{\Gamma} + \boldsymbol{\Sigma}_0^{-1}\right)^{-1}. \qquad (66)$$

---

[6] If we only know the typical value and spread of a parameter then a Gaussian is the maximum entropy prior (Jaynes 2003, section 7.11): the prior that is least informative given what we do know.

From this the inverse Fisher matrix $\boldsymbol{\Gamma}^{-1}$ is an upper bound on the size of the posterior covariance matrix.[7]

The Fisher matrix gives a quick way of estimating the range of posterior. It is widely used because of this. However, it is only appropriate when the approximation of (62) holds. This is known as the linearised-signal approximation (LSA), where higher order derivatives are neglected. To test the validity of this Vallisneri (2008) recommends use of the maximum-mismatch criterion

$$\ln r = -\frac{1}{2}\left(\Delta\lambda^a\partial_a\boldsymbol{h}_{\mathrm{ML}} - \Delta\boldsymbol{h}\middle|\Delta\lambda^b\partial_b\boldsymbol{h}_{\mathrm{ML}} - \Delta\boldsymbol{h}\right). \tag{67}$$

Here $\Delta\boldsymbol{\lambda}$ is the displacement to some point on the 1σ surface

$$\Delta\boldsymbol{\lambda} = \boldsymbol{\lambda}_{1\sigma} - \boldsymbol{\lambda}_{\mathrm{ML}}, \tag{68}$$

and $\Delta\boldsymbol{h}$ is the corresponding change in the waveform

$$\Delta\boldsymbol{h} = \boldsymbol{h}(\boldsymbol{\lambda}_{1\sigma}) - \boldsymbol{h}(\boldsymbol{\lambda}_{\mathrm{ML}}). \tag{69}$$

The 1σ surface is defined from the inverse of the Fisher matrix. If higher order terms are indeed negligible, then the maximum-mismatch criterion is small. We check this by picking a random selection of points on the 1σ surface, and evaluating $|\ln r|$. If this is smaller than a fiducial value, say $|\ln r| = 0.1$, over the majority, say 90%, of the surface we consider the LSA to be sufficiently justified.

We calculated Fisher matrices for a wide range of orbits and checked the maximum-mismatch criterion. We found that for the overwhelming majority of orbits the test failed: the LSA is not appropriate. This behaviour was seen even for orbits with $\rho \sim 10^3$–10^4.[8] Higher order terms are important, and cannot be neglected. EMRBs have a short duration and accordingly are not the most informative of signals. Therefore, the 1σ surface as defined by considering only the LSA terms is large. Taking such a large step in parameter space moves the signal beyond the region of linear changes.

We hope that this shall serve as an example to others. What constitutes high SNR depends upon the signal, it is not enough for $\rho > 1$. It is essential to check the maximum-mismatch criterion for individual waveforms: the threshold for the LSA to become applicable could be much greater than naively thought.

As we cannot be confident in Fisher matrix results, we opted to abandon this approach in favour of using Markov chain Monte Carlo simulations to explore constraints from different regions of parameter space. These are computationally more expensive, but they do not rely on any approximations. This avoids the heart-break of realising all your results are meaningless.

---

[7] It may also be shown to be the Cramér-Rao bound on the error covariance of an unbiased estimator (Cutler & Flanagan 1994; Vallisneri 2008). Thus it represents the frequentist error: the lower bound on the covariance for an unbiased parameter estimator $\boldsymbol{\lambda}_{\mathrm{est}}$ calculated from an infinite set of experiments with the same signal $\boldsymbol{h}(t)$ but different realisations of the noise $\boldsymbol{n}(t)$.

[8] In this study, to increase ρ we must reduce the periapse distance, this also reduces the region where the LSA is valid as parameter dependencies become more non-linear. If we had the luxury of increasing ρ by moving the GC closer, things could be different. Given the current economic climate, it seems unlikely that a mission to move the GC could be funded in the near future.

8.2 Markov chain Monte Carlo methods

Markov chain Monte Carlo (MCMC) methods are widely used for inference problems; they are a family of algorithms used for sampling an unknown probability distribution and are efficient for high-dimensional problems (MacKay 2003, chapter 29). Parameter space is explored by constructing randomly a chain of N samples. The distribution of points visited by the chain maps out the underlying distribution; this becomes asymptotically exact as $N \to \infty$. Samples are added sequentially, if the current state is $\boldsymbol{\lambda}_n$ a new point $\boldsymbol{\lambda}^*$ is drawn and accepted with probability

$$\mathcal{A} = \min\left\{\frac{\pi(\boldsymbol{\lambda}^*)\mathcal{L}(\boldsymbol{\lambda}^*)Q(\boldsymbol{\lambda}_n; \boldsymbol{\lambda}^*)}{\pi(\boldsymbol{\lambda}_n)\mathcal{L}(\boldsymbol{\lambda}_n)Q(\boldsymbol{\lambda}_n; \boldsymbol{\lambda}^*)}, 1\right\}, \tag{70}$$

setting $\boldsymbol{\lambda}_{n+1} = \boldsymbol{\lambda}^*$, where is the $\mathcal{L}(\boldsymbol{\lambda})$ likelihood, calculated in our case from (61); $\pi(\boldsymbol{\lambda})$ is the prior probability, and Q is a proposal distribution. If the move is not accepted we set $\boldsymbol{\lambda}_{n+1} = \boldsymbol{\lambda}_n$. This is the Metropolis-Hastings algorithm (Metropolis et al. 1953; Hastings 1970).

Simply waiting long enough shall yield an exact posterior. However, it is desirable for the MCMC to converge quickly. This requires a suitable choice for the proposal distribution. This can be difficult to define, since we do not know ahead of time the shape of the target distribution.

One approach to define the proposal distribution is to use the previous results in the chain, to refine the proposal by learning from these points. Such approaches are known as adaptive methods. Updating the proposal from previous points means that the chain is no longer truly Markovian. Care must be taken to ensure that ergodicity is preserved and convergence obtained (Roberts & Rosenthal 2007; Andrieu & Thoms 2008). To avoid this complication, we follow the suggestion of Haario et al. (1999), and use the adapting method as a burn in phase. We have an initial phase where the proposal is updated based upon the accepted points. After this we fix the proposal and proceed as for a standard MCMC. By only using samples from the second part, we guarantee that the chain is Markovian and ergodic, whilst still enjoying the benefits of a tailor-made proposal distribution. After only a finite number of samples we cannot assess the optimality of the proposal (Andrieu & Thoms 2008), but the method is still effective .

To tune the proposal, we use an approach based upon the adaptive Metropolis (AM) algorithm (Haario et al. 2001). The proposal is taken to be a multivariate normal distribution centred upon the current point, the covariance of which is taken to be

$$\boldsymbol{C} = s\left(\boldsymbol{V}_n + \varepsilon\boldsymbol{C}_0\right), \tag{71}$$

where $\boldsymbol{V}_n$ is the covariance of the accepted points $\{\boldsymbol{\lambda}_1, \ldots, \boldsymbol{\lambda}_n\}$, s is a scaling factor that controls the step size, ε is a small positive constant, typically taken to be 0.0025, and $\boldsymbol{C}_0$ is a constant matrix included to ensure ergodicity.

Our adaptation is run in three phases. The initial phase is just to get to get the chain moving. For this we set $\boldsymbol{C}_0^{\mathrm{init}} = \boldsymbol{I}_d$, where $\boldsymbol{I}_d$ is the identity. This finishes after 50000 accepted points.

For the second phase, we continue now using the proposal covariance from the initial phase $\boldsymbol{C}^{\mathrm{init}}$ for $\boldsymbol{C}_0^{\mathrm{main}}$. We reset the covariance of the accepted points $\boldsymbol{V}_n^{\mathrm{init}}$ so that it only includes points from this phase. This is the main

adaptation phase and lasts until 450000 points have been accepted.

In the final phase we restart the chain at the true parameter values. We no longer update the shape of the covariance ($\boldsymbol{V}_n$ remains fixed), but we adjust the step size s so as to tune the acceptance rate.

Throughout the adapting phases, we update the step size s after ever 100 trial points (whether or not they are accepted). When updating the covariance $\boldsymbol{V}_n$, this is done after every 1000 trial points.

We initially aimed for an acceptance rate of 0.234; this is optimal for a random walk Metropolis algorithm with some specific high-dimensional target distributions (Gelman et al. 1996; Roberts et al. 1997; Roberts & Rosenthal 2001; Bédard 2007). However, in many cases we found better convergence when aiming for a lower acceptance rate, say 0.1. This is not unexpected: the optimal rate may be lower than 0.234 when the parameters are not independent and identically distributed (Bédard 2007, 2008b,a). In practise, the final acceptance rate is (almost always) lower than the target rate as the use of a multivariate Gaussian for the proposal distribution is rarely a good fit at the edges of the posterior. Consequently, the precise choice for the target acceptance rate is unimportant as long as it is of the correct magnitude. Final rates are typically within a factor of 2 of the target value. As an initial choice, we set $s = 2.38^2/d$, which would be the optimal choice if $\boldsymbol{C}$ was the true target covariance for a high dimensional target of independent and identically distributed parameters (Gelman et al. 1996; Roberts et al. 1997; Roberts & Rosenthal 2001; Haario et al. 2001). Reasonably good results may be obtained by fixing s at this value, and not adjusting to fine tune the acceptance rate.

To assess the convergence of the MCMC we check the trace plot for proper mixing, that the one- and two-dimensional posterior plots fill out to a smooth distribution, and that the distribution widths tend towards consistent values.

9 RESULTS

9.1 Data set

To investigate the properties of EMRBs, waveforms were computed for a range of different orbits. In each case the massive black hole was assumed to have a mass of $M_\bullet = 4.31 \times 10^6 M_\odot$, and to be at the J2000.0 coordinates and a distance of $R_0 = 8.33$ kpc; the CO was chosen to be $10 M_\odot$, as the most promising candidates for EMRBs would be BHs.

Orbits where chosen with periapses uniformly distributed in logarithmic space between the MBH's event horizon and $16 r_g$. The other parameters were chosen randomly from appropriate uniform distributions.

The results of the MCMC runs illustrate why the Fisher matrix approach was insufficient. There are strong and complex parameter dependencies. For the many orbits the posteriors are far from Gaussian as assumed in the LSA.

These results do not incorporate any priors (save to keep them within realistic ranges). We have not folded in the existing information we have, for example, about the MBH's mass. Therefore, the resulting distributions characterise what we could learn from EMRB's alone. By the time

a space-bourne GW detector finally flies, we may well have much better constraints on some of the parameters.

It is possible to place good constraints from the closest orbits. These can provide sufficient information to give beautifully behaved posteriors although significant correlation between parameters persists.

Characteristic distribution widths are shown in Fig. 11. Plotted are the standard deviation σ_{SD}; a scaled 50-percentile range $\sigma_{50} = W_{50}/1.34898$, where W_{50} is the range that contains the median 50% of points, and a scaled 95-percentile range $\sigma_{95} = W_{95}/3.919928$, where W_{59} is the 95% range. The scaled ranges are such that all three widths are equal for a normal distribution. Filled circles are used for runs that appear to have converged. Open circles for those yet to converge, but which appear to be approaching an equilibrium state; widths are should be accurate to within a factor of a few. For guidance, dashed lines are included to indicate our current knowledge. This corresponds to the current measurement uncertainty for $M_\bullet$, and uniform priors for a_*, Φ_K, ϕ_p, χ_p, $cos\Theta_K$ and $\cos \iota$. We have no expectations on for the width of the MBH mass distribution with respect to the current value; however, we would expect that the recovered distributions for the other parameters are narrower than for the case of complete ignorance. This may not be the case if the distribution is multimodal: in this event using the width is an inadequate description of the distribution.

Comparing our MCMC results with Fisher matrix estimates, we see there can be a significant difference. The majority of parameters give results consistent to within an order of magnitude. The best agreement is for t_p, which is largely uncorrelated with the other parameters. The widths for $M_\bullet$, a_*, L_∞ and ι show more severe differences; these parameters show the tightest degeneracies. The two methods do show signs of slowly converging with increasing SNR, as expected.
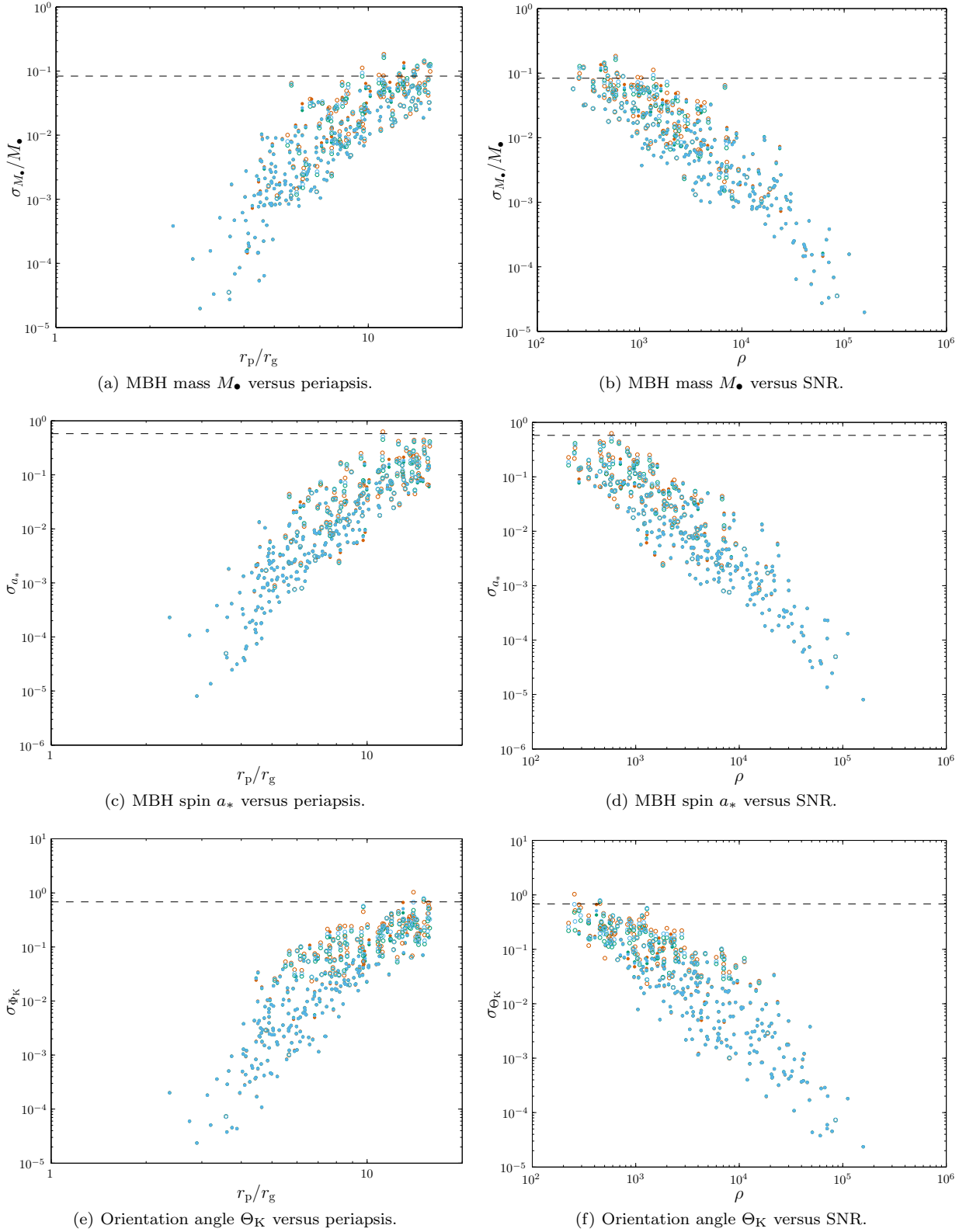
9.2 Comparison with existing results

Having quantified the accuracy with which we could hope to infer parameters from an EMRB waveform, we can now compare these results with existing measurements, to see if it is possible to learn anything new.
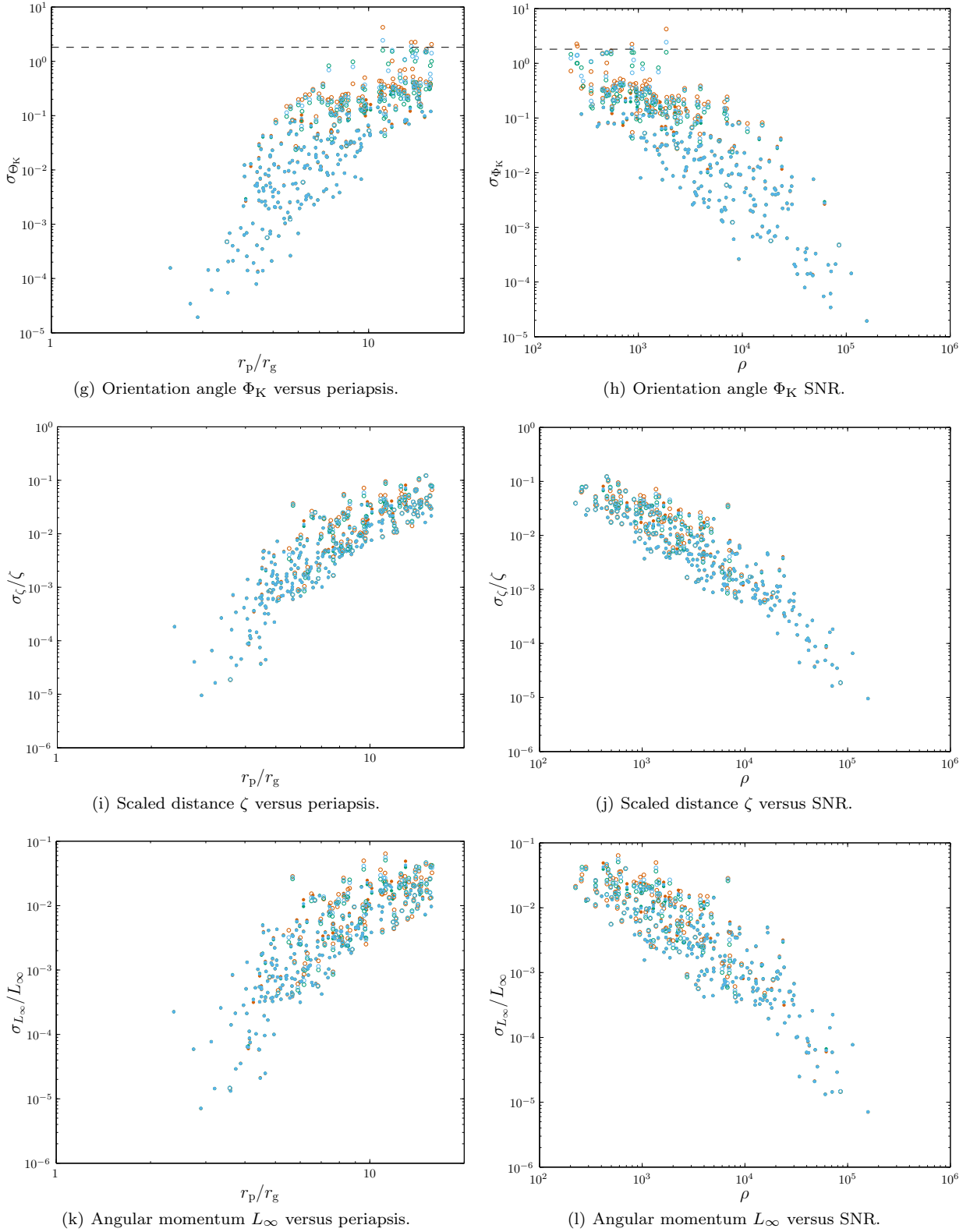
We have no *a priori* knowledge about the CO or its orbit, so anything we can deduce about its initial position, angular momentum or mass would be new. Measurements of the mass are only useful if σ_μ/μ is less than 1. From our power law, this would occur for a $1.4 M_\odot$ ($10 M_\odot$) object when $\rho \simeq 2.00$ (1.88). Since we would only expect to detect signals with SNRs of order of a few, we conclude that any detectable signal gives us some constraint on the compact object's mass. An uncertainty of 10% would be possible for $\rho \simeq 21.7$ (20.2).

Similarly, we have no information on the orientation of the MBH, so any measurement for which σ_Θ or σ_Ψ is less than 2π would be of interest. This happens for very low SNR for both angles, so again a detection would allow us to infer something new. An uncertainty of $\pi/72 = 5 \deg$ corresponds to $\rho \simeq 9.78$ (5.76) for Θ and $\rho \simeq 29.6$ (25.1) for Ψ.

We have existing measurements for the position of the MBH. The current constraints on $\overline{\Theta}$ and $\overline{\Phi}$ cannot be matched by observing EMRBs. The uncertainty in $\ln R_0$

(a) MBH mass $M_\bullet$ versus periapsis.

(b) MBH mass $M_\bullet$ versus SNR.

(c) MBH spin a_* versus periapsis.

(d) MBH spin a_* versus SNR.

(e) Orientation angle Θ_K versus periapsis.
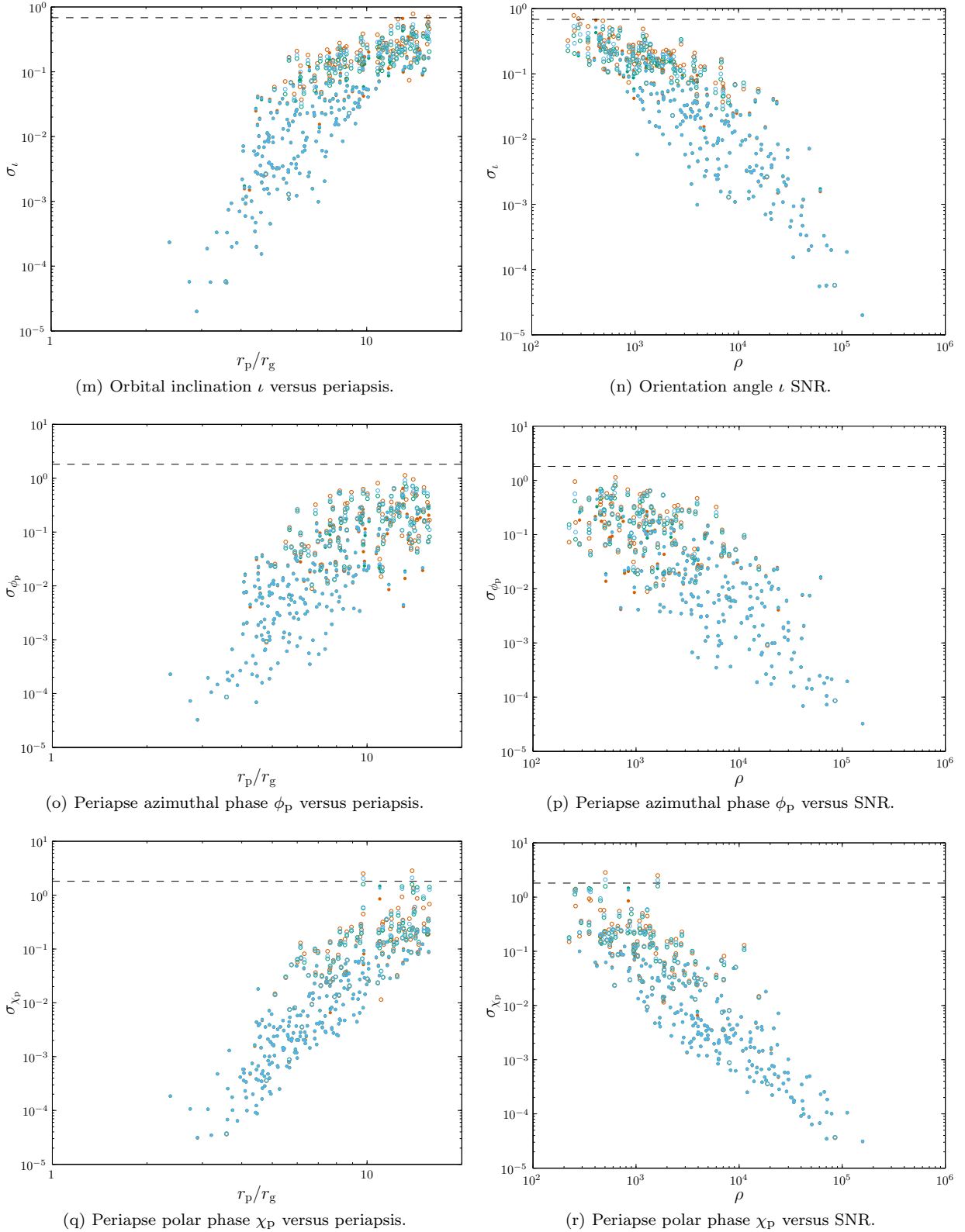
(f) Orientation angle Θ_K versus SNR.

Figure 11. Distribution widths as functions of periapse r_p and SNR ρ. Blue is used for the standard deviation, red is the scaled 50-percentile range and green is the scaled 95-percentile range: all three coincide for a normal distribution. Filled circles are used for converged runs, open circles for those yet to converge. The dashed line indicates the current uncertainty for $M_\bullet$, and the standard deviation for an uninformative prior for other parameters.

(g) Orientation angle Φ_K versus periapsis.

(h) Orientation angle Φ_K SNR.

(i) Scaled distance ζ versus periapsis.

(j) Scaled distance ζ versus SNR.

(k) Angular momentum L_∞ versus periapsis.
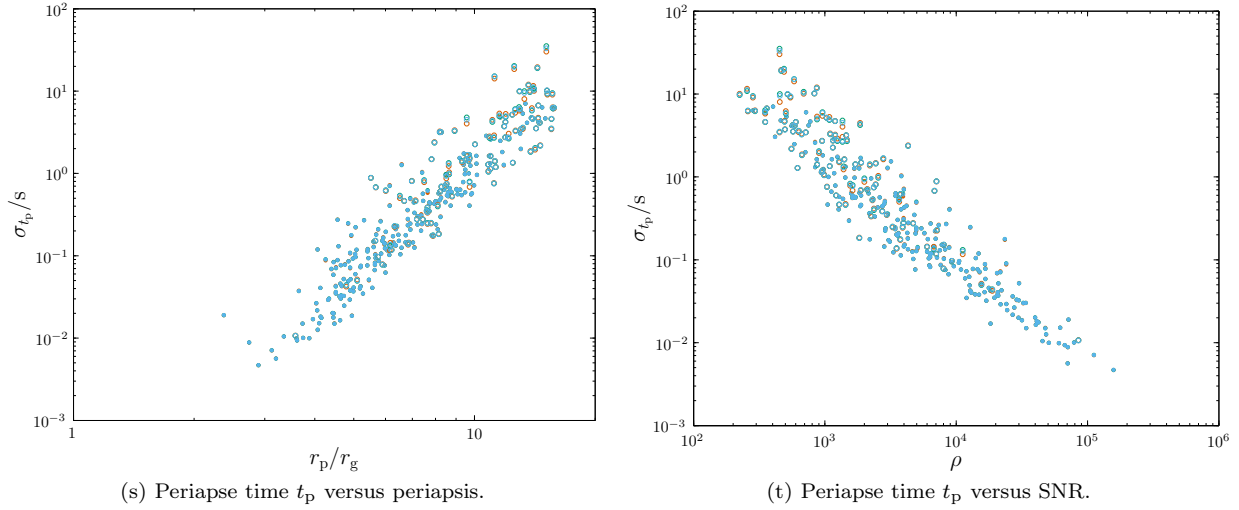
(l) Angular momentum L_∞ versus SNR.

Figure 11 – *continued* Distribution widths as functions of periapse r_p and SNR ρ. Blue is used for the standard deviation, red is the scaled 50-percentile range and green is the scaled 95-percentile range: all three coincide for a normal distribution. Filled circles are used for converged runs, open circles for those yet to converge. The dashed line indicates the current uncertainty for $M_\bullet$, and the standard deviation for an uninformative prior for other parameters.

(m) Orbital inclination ι versus periapsis.

(n) Orientation angle ι SNR.

(o) Periapse azimuthal phase $\phi_{\rm p}$ versus periapsis.

(p) Periapse azimuthal phase $\phi_{\rm p}$ versus SNR.

(q) Periapse polar phase $\chi_{\rm p}$ versus periapsis.

(r) Periapse polar phase $\chi_{\rm p}$ versus SNR.

Figure 11 – *continued* Distribution widths as functions of periapse $r_{\rm p}$ and SNR ρ. Blue is used for the standard deviation, red is the scaled 50-percentile range and green is the scaled 95-percentile range: all three coincide for a normal distribution. Filled circles are used for converged runs, open circles for those yet to converge. The dashed line indicates the current uncertainty for $M_\bullet$, and the standard deviation for an uninformative prior for other parameters.

(s) Periapse time t_p versus periapsis.

(t) Periapse time t_p versus SNR.

Figure 11 – *continued* Distribution widths as functions of periapse r_p and SNR ρ. Blue is used for the standard deviation, red is the scaled 50-percentile range and green is the scaled 95-percentile range: all three coincide for a normal distribution. Filled circles are used for converged runs, open circles for those yet to converge. The dashed line indicates the current uncertainty for $M_\bullet$, and the standard deviation for an uninformative prior for other parameters.

based on existing measurements is $\sigma_{\ln R_0}^0 \simeq 0.042$. This could be bettered by an EMRB with $\rho \simeq 2.68$ (2.75).

Of paramount interest are the MBH mass and spin. The current uncertainty in the mass is $\sigma_{M_\bullet}^0 = 0.36 \times 10^6 M_\odot$. This can be equalled for very low SNR, $\rho \simeq 0.11$ (0.12), so any detection should be able to improve measurement for $M_\bullet$. A 0.1% accuracy could be obtained for $\rho \approx 10.4$ (8.11).

The spin is less well known. To obtain an uncertainty of 0.1 would require $\rho \sim 23$ ($\simeq 51.1$) for $a_* = 0.0$; $\rho \sim 27$ ($\simeq 47.9$) for $a_* = 0.3$; $\rho \sim 28$ ($\simeq 48.3$) for $a_* = 0.6$, and $\rho \simeq 23.1$ ($\simeq 23.0$) for $a_* = 0.9$. We have used $\sim$ to denote values obtained using the higher SNR piece of the power-law, these values are much less accurate because of the large degree of scatter.

10   EXTRA-GALACTIC SOURCES

We have so far only been concerned with properties of bursts from our own galaxy. This is the best source for bursts because of its proximity. A natural continuation is to consider EMRBs from other MBHs. Rubbo et al. (2006) suggested that LISA should be able to detect EMRBs originating from the Virgo cluster, although the detectable rate may be only 10^{-4} yr^{-1} per galaxy (Hopman et al. 2007). Detectability depends upon the mass of the MBH; higher masses correspond to lower frequency bursts, which are harder to detect.

Checking our nearest neighbours, we find that bursts from Andromeda (M31) are not detectable. This is because of the large mass of the MBH $M_{M31} = (1.4^{+0.9}_{-0.3}) \times 10^8 M_\odot$ (Bender et al. 2005). However, its companion M32 is more promising. It has a lighter MBH $M_{M32} = (2.5 \pm 0.5) \times 10^6 M_\odot$ (Verolme et al. 2002). The trend between the periapse radius and SNR is shown in Fig. 12. The fit is again done for orbits with $f_* = \sqrt{GM_{M32}/r_p} < 1 \times 10^{-3}$ Hz to avoid the bucket of the noise curve. Bursts for a $1M_\odot$ ($10M_\odot$) can be detected if the periapse is smaller than $7r_g$ ($13r_g$).

We see that the general behaviour is the same as for
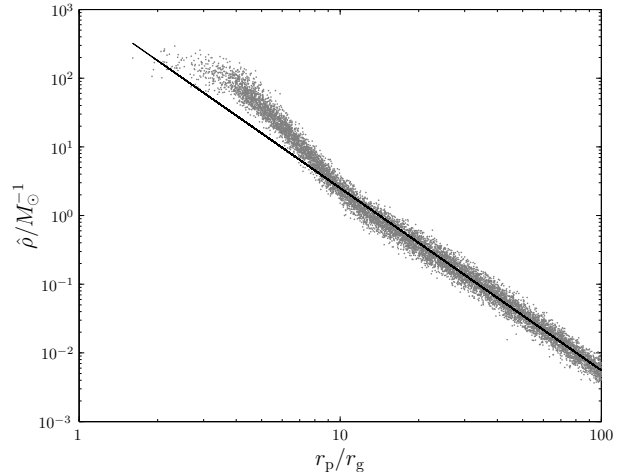
Figure 12. Signal-to-noise ratio as a function of periapse radius for a $\mu = 1M_\odot$ compact object about the MBH of M32. The plotted points are the values obtained by averaging over each set of intrinsic parameters. The best fit line is $\log(\rho) = -2.65 \log(r_p/r_g) + 3.05$. This is fitted to orbits with $r_p > 18.8r_g$ and has a reduced chi-squared value of $\chi^2/\nu = 1.26$.

the GC, but there are differences because of the position. Bursts from the two MBHs can be compared using the their characteristic frequencies f_* and scaled SNR

$$\rho_* = \rho \left(\frac{\mu}{M_\odot} \right)^{-1} \left(\frac{R}{\text{kpc}} \right) \left(\frac{M}{10^6 M_\odot} \right)^{-2/3}, \qquad (72)$$

where R and M are the appropriate distances and masses for the two MBHs. These scalings can be determined from the quadrupole piece of (26) assuming a characteristic length scale set by r_p. Figure 13 shows the trend for both galaxies. The difference in sky position is largely washed out through the motion of the the detector.

M31 and M32 are at a distance of 770 kpc (Karachentsev et al. 2004). It therefore seems unlikely that
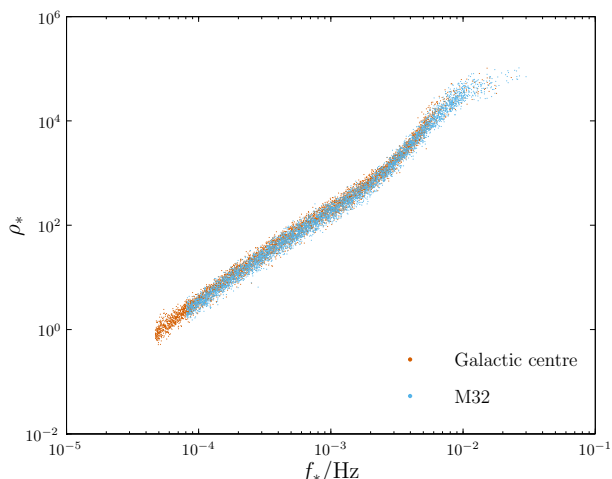
Figure 13. Scaled signal-to-noise ratio as a function of characteristic frequency.

bursts could be observed from the Virgo cluster at a distance of $R_{\rm Virgo} \approx 16.5$ Mpc (Mei et al. 2007).

Triangulum (M33) is believed to not have an MBH. Merritt et al. (2001) use dynamical constraints to place an upper bound on the mass of a central BH of $M_{\rm M33} < 3 \times 10^3 M_\odot$, Gebhardt et al. (2001) find a bound of $M_{\rm M33} < 1.5 \times 10^3 M_\odot$. Observations of the ultra-luminous nuclear X-ray source (ULX) closest to the centre of M33 yield a best estimate of $M_{\rm ULX} \sim \mathcal{O}(10) M_\odot$ for the source object's mass (Foschini et al. 2004; Weng et al. 2009). This is consistent with there being no MBH; the ULX originates from a stellar mass BH that is coincidentally located close to the core of the galaxy. Consequently, we do not expect to see any bursts from M33: to detect one would confirm the existence of a previously invisible MBH.

11 DISCUSSION

We have outlined an approximate method of generating gravitational waveforms for EMRBs originating at the GC. This assumes that the orbits are parabolic and employs a numerical kludge approximation. The two coordinate schemes for a NK presented here yield almost indistinguishable results. We conclude that either is a valid choice for this purpose. There may be differences of order 10% when the spin is large and the periapse is small ($r_{\rm p} \sim 4 r_{\rm g}$).

The waveforms created appear to be consistent with results obtained using Peters and Mathews waveforms for large periapses, indicating that they have the correct weak-field form. The NK approach should be superior to that of Peters and Mathews in the strong-field regime as it uses the exact geodesics of the Kerr spacetime. Comparisons with energy fluxes from black hole perturbation theory indicate that typical waveform accuracy may be of order 5%, but this is worse for orbits with small periapses, and may be $\sim 20\%$. These errors are much greater than the differences resulting from the use of the alternative coordinate systems.

The signal-to-noise ratio of bursts is well correlated with the periapsis. Except for the closest orbits ($r_{\rm p} \lesssim 7 r_{\rm g}$), the SNR (per unit mass) may be reasonably described as having

a power-law dependence of

$$\log\left(\hat{\rho}/M_\odot^{-1}\right) \simeq -2.7 \log(r_{\rm p}/r_{\rm g}) + 4.9. \tag{73}$$

Signals should be detectable for a $1 M_\odot$ ($10 M_\odot$) object if the periapse is $r_{\rm p} < 27 r_{\rm g}$ ($r_{\rm p} < 65 r_{\rm g}$), corresponding to a physical scale of 1.7×10^{11} m (4.1×10^{11} m) or 5.6×10^{-6} pc (1.3×10^{-5} pc).

Using the NK waveforms we conducted a trial investigation, using Fisher matrix analysis, into how accurately we could infer parameters of the galactic centre's MBH should such an EMRB be observed. However, we found that the LSA does not hold for these burst signals over a wide range of SNR. This demonstrates the necessity of checking the LSA before quoting the results of a Fisher matrix analysis (Vallisneri 2008).

Potentially, it is possible to determine very precisely the key parameters defining the MBH's mass and spin, if the orbit gets close enough to the MBH. From our investigation it appears that we can achieve good results from a single EMRB with periapsis of $r_{\rm p} \simeq X r_{\rm g}$ for a $10 M_\odot$ CO. This translates to a distance of $X \times 10^{11}$ m or $X \times 10^{-5}$ pc.

Before we can quote results for how accurately we can determine the various parameters, we must consider the probability of each orbit. This will be the subject of a companion paper, building upon the earlier results of Rubbo et al. (2006) and Hopman et al. (2007), who only considered approximate forms for the SNR, rather than using waveforms. Using a model for the nuclear star cluster of the GC it is possible to define distributions for angular momenta L_∞, for a species of mass μ. With these it is possible to estimate the event rate. This would allow us to estimate how much information, on average, we could hope to obtain from EMRB observations.

Some consideration should also be given to methods of fitting a waveform to an observed signal. Given a noisy data stream, how could EMRBs be extracted? The parabolic spectrum has a characteristic profile, suggesting that matched filtering could be possible. Complications could arise in fitting parameters to a waveform: we have seen that there exist complicated degeneracies between parameters. These issues would warrant further investigation should the event rate be high enough.

While we have only considered bursts from our own galaxy in detail, it should be possible to observe bursts from other nearby galaxies if their MBH is of the appropriate mass. This leaves M32 as the only viable known candidate. The SNR shows a similar dependence upon periapsis as for the Galactic Centre, and may be described by a power-law of

$$\log\left(\hat{\rho}/M_\odot^{-1}\right) \simeq -2.7 \log(r_{\rm p}/r_{\rm g}) + 3.1, \tag{74}$$

for orbits with $r_{\rm p} \gtrsim 10 r_{\rm g}$. For a $1 M_\odot$ ($10 M_\odot$) object, bursts should be detectable for periapses $r_{\rm p} \lesssim 7 r_{\rm g}$ ($r_{\rm p} \lesssim 14 r_{\rm g}$), corresponding to 2.6×10^{10} m (4.9×10^{10} m) or 8.4×10^{-7} pc (1.6×10^{-6} pc). This is a small region of parameter space, so we conclude that extra-galactic bursts shall be rare.

REFERENCES

Amaro-Seoane P., Aoudia S., Babak S., Binetruy P., Berti E., Bohe A., 2012, p. 20

Amaro-Seoane P., Gair J. R., Freitag M., Miller M. C., Mandel I., Cutler C. J., Babak S., 2007, Classical and Quantum Gravity, 24, R113

Andrieu C., Thoms J., 2008, Statistics and Computing, 18, 343

Babak S., Fang H., Gair J., Glampedakis K., Hughes S., 2007, Physical Review D, 75, 024005

Backer D. C., Sramek R. A., 1999, The Astrophysical Journal, 524, 805

Barack L., Cutler C., 2004, Physical Review D, 69, 082005

Bédard M., 2007, The Annals of Applied Probability, 17, 1222

Bédard M., 2008a, Journal of Computational and Graphical Statistics, 17, 312

Bédard M., 2008b, Stochastic Processes and their Applications, 118, 2198

Bekenstein J. D., 1973, The Astrophysical Journal, 183, 657

Bélanger G., Terrier R., de Jager O. C., Goldwurm A., Melia F., 2006, Journal of Physics: Conference Series, 54, 420

Bender P., Brillet A., Ciufolini I., Cruise A. M., Cutler C., Danzmann K., 1998, Technical report, LISA Pre-Phase A Report. Max-Planck-Institut für Quantenoptik, Garching

Bender R., Kormendy J., Bower G., Green R., Thomas J., Danks A. C., Gull T., Hutchings J. B., Joseph C. L., Kaiser M. E., Lauer T. R., Nelson C. H., Richstone D., Weistrop D., Woodgate B., 2005, The Astrophysical Journal, 631, 280

Berry C. P. L., Gair J. R., 2010, Physical Review D, 82, 107501

Berti E., Cardoso V., Gonzalez J. A., Sperhake U., Hannam M., Husa S., Brügmann B., 2007, Physical Review D, 76, 064034

Berti E., Volonteri M., 2008, The Astrophysical Journal, 684, 822

Boyer R. H., Lindquist R. W., 1967, Journal of Mathematical Physics, 8, 265

Brenneman L. W., Reynolds C. S., 2006, The Astrophysical Journal, 652, 1028

Burko L. M., Khanna G., 2007, EPL, 78, 60005

Carter B., 1968, Physical Review, 174, 1559

Carter B., 1971, Physical Review Letters, 26, 331

Chandrasekhar S., 1998, The Mathematical Theory of Black Holes. Oxford Classic Texts in the Physical Sciences, Oxford University Press, Oxford

Cutler C., 1998, Physical Review D, 57, 7089

Cutler C., Flanagan E. E., 1994, Physical Review D, 49, 2658

Damour T., Iyer B. R., Sathyaprakash B. S., 2000, Physical Review D, 62, 084036

Danzmann K., Rüdiger A., 2003, Classical and Quantum Gravity, 20, S1

de Felice F., 1980, Journal of Physics A: Mathematical and General, 13, 1701

de la Calle Pérez I., Longinotti A. L., Guainazzi M., Bianchi S., Dovčiak M., Cappi M., Matt G., Miniutti G., Petrucci P. O., Piconcelli E., Ponti G., Porquet D., Santos-Lleó M., 2010, Astronomy & Astrophysics, 524, A50

Doeleman S. S., Weintroub J., Rogers A. E. E., Plambeck R., Freund R., 2008, Nature, 455, 78

Drasco S., Hughes S., 2004, Physical Review D, 69, 044015

Ferrarese L., Merritt D., 2000, The Astrophysical Journal, 539, L9

Finn L. S., 1992, Physical Review D, 46, 5236

Foschini L., Rodriguez J., Fuchs Y., Ho L. C., Dadina M., Di Cocco G., Courvoisier T. J.-L., Malaguti G., 2004, Astronomy and Astrophysics, 416, 529

Gair J. R., Kennefick D. J., Larson S. L., 2005, Physical Review D, 72, 084009

Gammie C. F., Shapiro S. L., McKinney J. C., 2004, The Astrophysical Journal, 602, 312

Gebhardt K., Bender R., Bower G., Dressler A., Faber S. M., Filippenko A. V., Green R., Grillmair C., Ho L. C., Kormendy J., Lauer T. R., Magorrian J., Pinkney J., Richstone D., Tremaine S., 2000, The Astrophysical Journal, 539, L13

Gebhardt K., Lauer T. R., Kormendy J., Pinkney J., Bower G. A., Green R., Gull T., Hutchings J. B., Kaiser M. E., Nelson C. H., Richstone D., Weistrop D., 2001, The Astronomical Journal, 122, 2469

Gelman A., Roberts G. O., Gilks W. R., 1996, in Bernardo J. M., Berger J. O., Dawid A. P., Smith A. F. M., eds, Bayesian Statistics Valencia International Meeting, Efficient Metropolis jumping Rules. Oxford University Press, Oxford, pp 599–607

Genzel R., Schödel R., Ott T., Eckart A., Alexander T., Lacombe F., Rouan D., Aschenbach B., 2003, Nature, 425, 934

Ghez A. M., Salim S., Weinberg N. N., Lu J. R., Do T., Dunn J. K., Matthews K., Morris M. R., Yelda S., Becklin E. E., Kremenek T., Milosavljevic M., Naiman J., 2008, The Astrophysical Journal, 689, 1044

Gillessen S., Eisenhauer F., Trippe S., Alexander T., Genzel R., Martins F., Ott T., 2009, The Astrophysical Journal, 692, 1075

Glampedakis K., 2005, Classical and Quantum Gravity, 22, S605

Glampedakis K., Hughes S., Kennefick D., 2002, Physical Review D, 66, 064005

Glampedakis K., Kennefick D., 2002, Physical Review D, 66, 044002

González J. A., Sperhake U., Brügmann B., Hannam M., Husa S., 2007, Physical Review Letters, 98, 091101

Graham A. W., 2007, Monthly Notices of the Royal Astronomical Society, 379, 711

Graham A. W., Erwin P., Caon N., Trujillo I., 2001, The Astrophysical Journal, 563, L11

Graham A. W., Onken C. A., Athanassoula E., Combes F., 2011, Monthly Notices of the Royal Astronomical Society, 412, 2211

Haario H., Saksman E., Tamminen J., 1999, Computational Statistics, 14, 375

Haario H., Saksman E., Tamminen J., 2001, Bernoulli, 7, 223

Haiman Z., Quataert E., 2004, The Formation and Evolution of the First Massive Black Holes. Kluwer Academic Publishers, Dordrecht, pp 147–186

Hamaus N., Paumard T., Müller T., Gillessen S., Eisenhauer F., Trippe S., Genzel R., 2009, The Astrophysical Journal, 692, 902

Häring N., Rix H.-W., 2004, The Astrophysical Journal, 604, L89

Harris F., 1978, Proceedings of the IEEE, 66, 51

Hastings W. K., 1970, Biometrika, 57, 97

Hawking S. W., 1972, Communications in Mathematical Physics, 25, 152

Hobson M. P., Efstathiou G., Lasenby A., 2006, General Relativity: An Introduction for Physicists. Cambridge University Press, Cambridge

Hopman C., Freitag M., Larson S. L., 2007, Monthly Notices of the Royal Astronomical Society, 378, 129

Hughes S. A., Blandford R. D., 2003, The Astrophysical Journal, 585, L101

Israel W., 1967, Physical Review, 164, 1776

Israel W., 1968, Communications in Mathematical Physics, 8, 245

Jahnke K., Macciò A. V., 2011, The Astrophysical Journal, 734, 92

Jaynes E. T., 2003, Probability Theory: The Logic of Science. Cambridge University Press, Cambridge

Jennrich O., Binetruy P., Colpi M., Danzmann K., Jetzer P., Lobo A., 2011, Technical report, NGO Revealing a hidden Universe: opening a new chapter of discovery. European Space Agency

Kaiser J., Schafer R., 1980, Acoustics, Speech and Signal Processing, IEEE Transactions on, 28, 105

Karachentsev I. D., Karachentseva V. E., Huchtmeier W. K., Makarov D. I., 2004, The Astronomical Journal, 127, 2031

Kato Y., Miyoshi M., Takahashi R., Negoro H., Matsumoto R., 2010, Monthly Notices of the Royal Astronomical Society: Letters, 403, L74

Kerr R., 1963, Physical Review Letters, 11, 237

King A. R., Pringle J. E., 2006, Monthly Notices of the Royal Astronomical Society: Letters, 373, L90

King A. R., Pringle J. E., Hofmann J. A., 2008, Monthly Notices of the Royal Astronomical Society, 385, 1621

Kormendy J., Richstone D., 1995, Annual Review of Astronomy and Astrophysics, 33, 581

Larson S. L., Hellings R. W., Hiscock W. A., 2002, Physical Review D, 66, 062001

Larson S. L., Hiscock W. A., Hellings R. W., 2000, Physical Review D, 62, 062001

Lynden-Bell D., Rees M. J., 1971, Monthly Notices of the Royal Astronomical Society, 152, 461

McClintock J. E., Narayan R., Davis S. W., Gou L., Kulkarni A., Orosz J. A., Penna R. F., Remillard R. A., Steiner J. F., 2011, Classical and Quantum Gravity, 28, 114009

MacKay D. J. C., 2003, Information Theory, Inference and Learning Algorithms. Cambridge University Press, Cambridge

McKechan D. J. A., Robinson C., Sathyaprakash B. S., 2010, Classical and Quantum Gravity, 27, 084020

Magorrian J., Tremaine S., Richstone D., Bender R., Bower G., Dressler A., Faber S. M., Gebhardt K., Green R., Grillmair C., Kormendy J., Lauer T., 1998, The Astronomical Journal, 115, 2285

Malbon R. K., Baugh C. M., Frenk C. S., Lacey C. G., 2007, Monthly Notices of the Royal Astronomical Society, 382, 1394

Marconi A., Hunt L. K., 2003, The Astrophysical Journal, 589, L21

Martel K., 2004, Physical Review D, 69, 044025

Mei S., Blakeslee J. P., Cote P., Tonry J. L., West M. J., Ferrarese L., Jordan A., Peng E. W., Anthony A., Merritt D., 2007, The Astrophysical Journal, 655, 144

Merritt D., Alexander T., Mikkola S., Will C. M., 2010, Physical Review D, 81, 062002

Merritt D., Ferrarese L., Joseph C. L., 2001, Science, 293, 1116

Metropolis N., Rosenbluth A. W., Rosenbluth M. N., Teller A. H., Teller E., 1953, The Journal of Chemical Physics, 21, 1087

Miller J., 2007, Annual Review of Astronomy and Astrophysics, 45, 441

Miniutti G., Panessa F., De Rosa A., Fabian A. C., Malizia A., Molina M., Miller J. M., Vaughan S., 2009, Monthly Notices of the Royal Astronomical Society, 398, 255

Misner C. W., Thorne K. S., Wheeler J. A., 1973, Gravitation. W. H. Freeman, New York

Nardini E., Fabian A. C., Reis R. C., Walton D. J., 2011, Monthly Notices of the Royal Astronomical Society, 410, 1251

Nuttall A., 1981, IEEE Transactions on Acoustics, Speech and Signal Processing, 29, 84

Patrick A. R., Reeves J. N., Porquet D., Markowitz A. G., Lobban A. P., Terashima Y., 2011, Monthly Notices of the Royal Astronomical Society, 411, 2353

Peng C. Y., 2007, The Astrophysical Journal, 671, 1098

Peters P. C., 1964, Physical Review, 136, B1224

Peters P. C., Mathews J., 1963, Physical Review, 131, 435

Press W., 1977, Physical Review D, 15, 965

Psaltis D., 2008, Living Reviews in Relativity, 11

Rees M. J., 1984, Annual Review of Astronomy and Astrophysics, 22, 471

Reid M. J., Menten K. M., Genzel R., Ott T., Schödel R., Brunthaler A., 2003, Astronomische Nachrichten, 324, 505

Reid M. J., Readhead A. C. S., Vermeulen R. C., Treuhaft R. N., 1999, The Astrophysical Journal, 524, 816

Roberts G. O., Gelman A., Gilks W. R., 1997, The Annals of Applied Probability, 7, 110

Roberts G. O., Rosenthal J. S., 2001, Statistical Science, 16, 351

Roberts G. O., Rosenthal J. S., 2007, Journal of Applied Probability, 44, 458

Robinson D., 1975, Physical Review Letters, 34, 905

Rosquist K., Bylund T., Samuelsson L., 2009, International Journal of Modern Physics D, 18, 429

Rubbo L. J., Holley-Bockelmann K., Finn L. S., 2006, The

Astrophysical Journal, 649, L25

Ruffini R., Sasaki M., 1981, Progress of Theoretical Physics, 66, 1627

Sathyaprakash B., Schutz B. F., 2009, Living Reviews in Relativity, 12

Schmoll S., Miller J. M., Volonteri M., Cackett E., Reynolds C. S., Fabian A. C., Brenneman L. W., Miniutti G., Gallo L. C., 2009, The Astrophysical Journal, 703, 2171

Sikora M., Stawarz L., Lasota J.-P., 2007, The Astrophysical Journal, 658, 815

Sołtan A., 1982, Monthly Notices of the Royal Astronomical Society, 200, 115

Tanaka T., Shibata M., Sasaki M., Tagoshi H., Nakamura T., 1993, Progress of Theoretical Physics, 90, 65

Thorne K. S., 1974, The Astrophysical Journal, 191, 507

Tremaine S., Gebhardt K., Bender R., Bower G., Dressler A., Faber S. M., Filippenko A. V., Green R., Grillmair C., Ho L. C., Kormendy J., Lauer T. R., Magorrian J., Pinkney J., Richstone D., 2002, The Astrophysical Journal, 574, 740

Trippe S., Paumard T., Ott T., Gillessen S., Eisenhauer F., Martins F., Genzel R., 2007, Monthly Notices of the Royal Astronomical Society, 375, 764

Turner M., 1977, The Astrophysical Journal, 216, 610

Vallisneri M., 2008, Physical Review D, 77, 042001

Verolme E. K., Cappellari M., Copin Y., van der Marel R. P., Bacon R., Bureau M., Davies R. L., Miller B. M., de Zeeuw P. T., 2002, Monthly Notices of the Royal Astronomical Society, 335, 517

Volonteri M., 2010, The Astronomy and Astrophysics Review, 18, 279

Volonteri M., Madau P., Quataert E., Rees M. J., 2005, The Astrophysical Journal, 620, 69

Volonteri M., Natarajan P., 2009, Monthly Notices of the Royal Astronomical Society, 400, 1911

Volonteri M., Sikora M., Lasota J.-P., 2007, The Astrophysical Journal, 667, 704

Weng S.-S., Wang J.-X., Gu W.-M., Lu J.-F., 2009, Publications of the Astronomical Society of Japan, 61, 1287

Wilkins D., 1972, Physical Review D, 5, 814

Yu Q., Tremaine S., 2002, Monthly Notices of the Royal Astronomical Society, 335, 965

Yunes N., Sopuerta C. F., Rubbo L. J., Holley-Bockelmann K., 2008, The Astrophysical Journal, 675, 604

Yusef-Zadeh F., Choate D., Cotton W., 1999, The Astrophysical Journal, 518, L33

Zoghbi A., Fabian A. C., Uttley P., Miniutti G., Gallo L. C., Reynolds C. S., Miller J. M., Ponti G., 2010, Monthly Notices of the Royal Astronomical Society, 401, 2419

APPENDIX A: WINDOW FUNCTIONS

When performing a Fourier transform using a computer we must necessarily only transform a finite time-span τ. The effect of this is the same as transforming the true, infinite signal multiplied by a unit top-hat function of width equal to the time-span. Transforming this yields the true waveform convolved with a sinc. If $\tilde{h}'(f)$ is the computed Fourier transform then

$$\tilde{h}'(f) = \int_{-\tau/2}^{\tau/2} h(t)e^{2\pi ift}\,\mathrm{d}t = \left[\tilde{h}(f) * \tau \operatorname{sinc}(\pi f\tau) \right], \qquad (A1)$$

where $\tilde{h}(f) = \mathscr{F}\{h(t)\}$ is the unwindowed Fourier transform of the infinite signal. This windowing of the data is a problem innate in the method and results in spectral leakage.

Figure 1(a) shows the computed Fourier transform for an example EMRB. The waveform has two distinct regions: a low-frequency curve, and a high-frequency tail. The low-frequency signal is the spectrum we are interested in; the high-frequency components are a combination of spectral leakage and numerical noise. The $\mathcal{O}(1/f)$ behaviour of the sinc gives the shape of the tail. This has possibly been misidentified in figure 8 of Burko & Khanna (2007) as the characteristic strain for parabolic encounters.

Despite being many orders of magnitude below the peak level, the high-frequency tail is still well above the noise curve for a wide range of frequencies. It therefore contributes to the evaluation of any inner products, and could mask interesting features. It is possible to reduce the amount of leakage using apodization: to improve the frequency response of a finite time series one can use a weighting window function $w(t)$ which modifies the impulse response in a prescribed way.

The simplest window function is the rectangular (or Dirichlet) window $w_{\mathrm{R}}(t)$; this is just the top-hat described above. Other window functions are generally tapered.[9] There is a wide range of window functions described in the literature (Harris 1978; Kaiser & Schafer 1980; Nuttall 1981; McKechan, Robinson & Sathyaprakash 2010). The introduction of a window function influences the spectrum in a manner dependent upon its precise shape. There are two distinct distortions: local smearing due to the finite width of the centre lobe, and distant leakage due to finite amplitude sidelobes. The window function may be optimised such that the peak sidelobe has a small amplitude, or such that the sidelobes decay away rapidly with frequency. Choosing a window function is a trade-off between these various properties, and shall depend upon the particular application.

For use with the parabolic spectra, the primary concern is to suppress the sidelobes. Many windows with good sidelobe behaviour exist; we consider three: the Blackman-Harris minimum four-term window (Harris 1978; Nuttall 1981)

$$w_{\mathrm{BH}}(t) = \sum_{n=0}^{3} a_n^{\mathrm{BH}} \cos\left(\frac{2n\pi t}{\tau}\right), \qquad (A2)$$
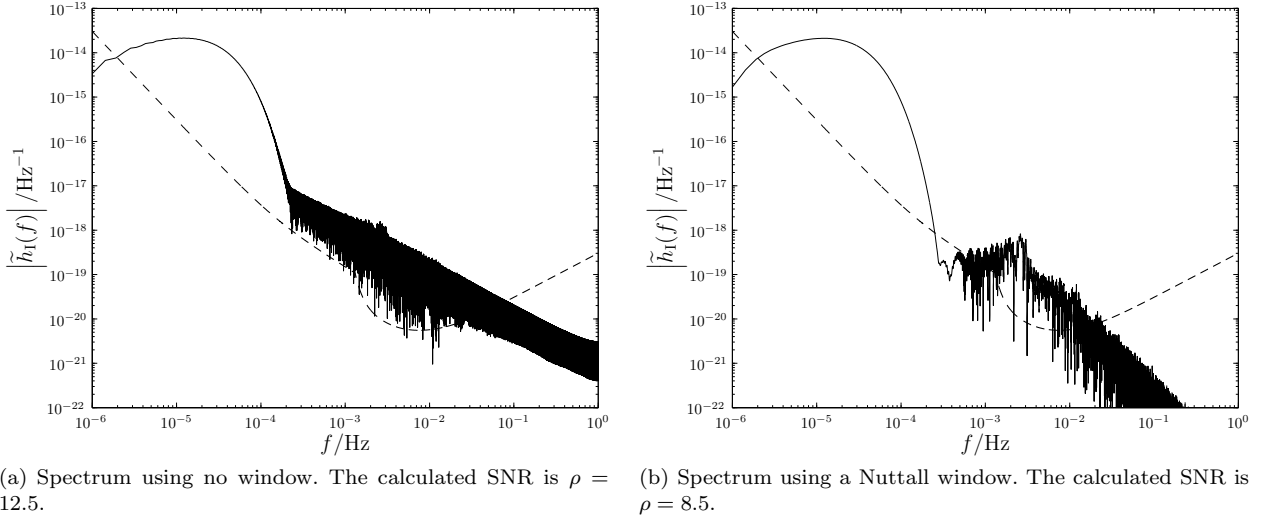
where

$$\begin{aligned} a_0^{\mathrm{BH}} &= 0.35875, \quad a_1^{\mathrm{BH}} = 0.48829, \\ a_2^{\mathrm{BH}} &= 0.14128, \quad a_3^{\mathrm{BH}} = 0.01168; \end{aligned} \qquad (A3)$$

the Nuttall four-term window with continuous first derivative (Nuttall 1981)

$$w_{\mathrm{N}}(t) = \sum_{n=0}^{3} a_n^{\mathrm{N}} \cos\left(\frac{2n\pi t}{\tau}\right), \qquad (A4)$$

---

[9] When using a tapered window function it is important to ensure that the window is centred upon the signal; otherwise the calculated transform shall have a reduced amplitude.

(a) Spectrum using no window. The calculated SNR is $\rho = 12.5$.

(b) Spectrum using a Nuttall window. The calculated SNR is $\rho = 8.5$.

Figure A1. Example spectra calculated using (a) a rectangular window and (b) Nuttall's four-term window with continuous first derivative (Nuttall 1981). The spin of the MBH is $a_* = 0.5$, the mass of the orbiting CO is $\mu = 10 M_\odot$, the periapsis is $r_p = 50 r_g$ and the inclination is $\iota = 0.1$. The high-frequency tail is the result of spectral leakage. The level of the LISA noise curve is indicated by the dashed line. The spectra are from detector I, detector II has similar spectra.

where

$$a_0^N = 0.355768, \quad a_1^N = 0.487396,$$
$$a_2^N = 0.144232, \quad a_3^N = 0.012604, \tag{A5}$$

and the Kaiser-Bessel window (Harris 1978; Kaiser & Schafer 1980)

$$w_{KB}(t; \beta) = \frac{I_0 \left[\beta \sqrt{1 - (2t/\tau)^2} \right]}{I_0(\beta)}, \tag{A6}$$

where $I_\nu(z)$ is the modified Bessel function of the first kind, and β is an adjustable parameter. Increasing β reduces the peak sidelobe, but also widens the central lobe.

The Kaiser-Bessel window has the smallest peak sidelobe, but the worst decay ($1/f$); the Nuttall window has the best asymptotic behaviour ($1/f^3$); the Blackman-Harris window has a peak sidelobe similar to the Nuttall window, and decays asymptotically as fast (slow) as the Kaiser-Bessel window, but has the advantage of having suppressed sidelobes next to the central lobe.
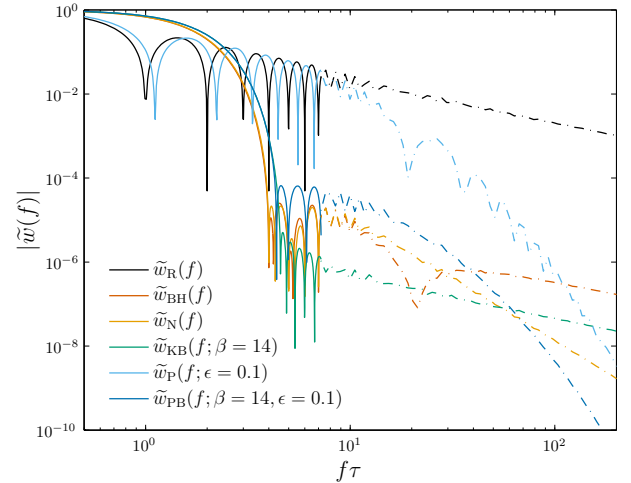
Another window has been recently suggested for use with gravitational waveforms: the Planck-taper window (Damour, Iyer & Sathyaprakash 2000; McKechan et al. 2010)

$$w_P(t; \epsilon) = \begin{cases} \dfrac{1}{\exp(Z_+) + 1} & -\dfrac{\tau}{2} \leqslant t < -\tau\left(\dfrac{1}{2} - \epsilon\right) \\ 1 & -\tau\left(\dfrac{1}{2} - \epsilon\right) < t < \tau\left(\dfrac{1}{2} - \epsilon\right) \\ \dfrac{1}{\exp(Z_-) + 1} & -\tau\left(\dfrac{1}{2} - \epsilon\right) < t \leqslant \dfrac{\tau}{2} \end{cases}, \tag{A7}$$

with

$$Z_\pm(t; \epsilon) = 2\epsilon \left[\frac{1}{1 \pm 2(t/\tau)} + \frac{1}{1 - 2\epsilon \pm 2(t/\tau)} \right]. \tag{A8}$$

This was put forward for use with binary coalescences, and

Figure A2. Window function frequency response. To avoid clutter, the response function is only plotted in detail until $f\tau = 8$, above this a smoothed value is used, as indicated by the dot-dashed line. As well as having good asymptotic behaviour, the Planck-taper window has the narrowest main lobe, except for the rectangular window.

has superb asymptotic decay. However, the peak sidelobe is high, which is disadvantageous here. We therefore propose a new window function: the Planck-Bessel window which combines the Kaiser-Bessel and Planck-taper windows to produce a window which inherits the best features of both, albeit in a diluted form,

$$w_{PB}(t; \beta, \epsilon) = w_P(t; \epsilon) w_{KB}(t; \beta). \tag{A9}$$

The window functions' frequency responses are plotted in Fig. A2. There is no window that performs best everywhere.

Figure A1 shows the computed Fourier transforms for an example EMRB using no window (alternatively a rectan-

gular window), and the Nuttall window.[10] Using the Nuttall window, the spectral leakage is greatly reduced; the peak sidelobe is lower, and the tail decays away as $1/f^3$ instead of $1/f$. The low frequency signal is not appreciably changed.

The choice of window function influences the results as it changes the form of $\widetilde{h}(f)$. The variation in results between windows depends upon the signal: variation is greatest for low frequency bursts, as then there is greatest scope for leakage into the detector frequency band; variation is least significant for zoom-whirl orbits as then there are strong signals to relatively high frequencies, and spectral leakage is confined to mostly below the noise level. To quantify the influence of window functions, we studied the diagonal elements of the Fisher matrix from a selection of orbits with periapses ranging from $\sim 10 r_\mathrm{g}$–$300 r_\mathrm{g}$. For orbits with small periapses all five windows (excluding the rectangular window) produced very similar results: the Planck-taper window differed by a maximum of $\sim 0.5\%$ from the others, which all agreed to better than 0.1%. The worst case results came from the lowest frequency orbits, then the Planck-taper window deviated by a maximum of $\sim 30\%$ in the value for the Fisher matrix elements, the Blackman-Harris deviated by $\sim 20\%$ and the others agreed to better than $\sim 5\%$. The Planck-taper window's performance is limited by its poor sidelobe behaviour; the Blackman-Harris has the worst performance at high frequency.

For this work we have used the Nuttall window. Its performance is comparable to the Kaiser-Bessel and Planck-Bessel windows, but it is computationally less expensive to implement as it does not contain Bessel functions. Results should be accurate to a few percent at worst, and results from closer orbits, which provide better constraints, should be less affected by the choice of window function. Therefore, we are confident that none of our conclusions are sensitive to the particular windowing method implemented.

This paper has been typeset from a TEX/ LATEX file prepared by the author.

---

[10] The Blackman-Harris, Kaiser-Bessel and Planck-Bessel windows give almost identical results.